

The HERMES Recoil Detector

A. Airapetian^{k,n}, E. C. Aschenauer^{e,1}, S. Belostotski^p, A. Borissov^{d,l}, A. Borisenkoⁱ, J. Bowles^l, I. Brodski^k, V. Bryzgalov^q, J. Burns^l, G. P. Capitaniⁱ, V. Carassiti^h, G. Ciullo^h, A. Clarkson^l, M. Contalbrigo^h, R. De Leo^a, E. De Sanctisⁱ, M. Diefenthaler^{m,g}, P. Di Nezzaⁱ, M. Düren^k, M. Ehrenfried^{k,2}, H. Guler^d, I. M. Gregor^d, M. Hartig^d, G. Hill^l, M. Hoek^{l,k}, Y. Holler^d, I. Hristova^e, H. S. Jo^j, R. Kaiser^{l,3}, T. Keri^{l,k}, A. Kisselev^p, B. Krause^d, B. Krauss^{g,4}, L. Lagamba^a, I. Lehmann^{l,5}, P. Lenisa^h, S. Lu^k, X.-G. Lu^e, S. Lumsden^l, D. Mahon^l, A. Martinez de la Ossa^b, M. Murray^l, A. Mussgiller^{d,g}, W.-D. Nowak^e, Y. Naryshkin^p, A. Osborne^l, L. L. Pappalardo^h, R. Perez-Benito^k, A. Petrov^d, N. Pickert^{g,4}, V. Prah^d, D. Protopopescu^l, M. Reinecke^d, C. Riedl^{e,m}, K. Rith^g, G. Rosner^l, L. Rubacek^k, D. Ryckbosch^j, Y. Salomatin^q, G. Schnell^{c,j}, B. Seitz^l, C. Shearer^l, V. Shutov^f, M. Statera^h, J. J. M. Steijger^o, H. Stenzel^k, J. Stewart^{e,1}, F. Stinzinger^g, A. Trzcinski^r, M. Tytgat^j, A. Vandenbroucke^{j,6}, Y. Van Haarlem^{j,7}, C. Van Hulse^{c,j}, M. Varanda^d, D. Veretennikov^p, I. Vilardi^{a,8}, V. Vikhrov^p, C. Vogel^{g,9}, S. Yaschenko^{d,g}, Z. Ye^{e,10}, W. Yu^k, D. Zeiler^{g,2} and B. Zihlmann^{j,11}

^aIstituto Nazionale di Fisica Nucleare, Sezione di Bari, 70124 Bari, Italy

^bNuclear Physics Laboratory, University of Colorado, Boulder, Colorado 80309-0390, USA

^cDepartment of Theoretical Physics, University of the Basque Country UPV/EHU, 48080 Bilbao, Spain and IKERBASQUE, Basque Foundation for Science, 48011 Bilbao, Spain

^dDESY, 22603 Hamburg, Germany

^eDESY, 15738 Zeuthen, Germany

^fJoint Institute for Nuclear Research, 141980 Dubna, Russia

^gPhysikalisches Institut, Universität Erlangen-Nürnberg, 91058 Erlangen, Germany

^hIstituto Nazionale di Fisica Nucleare, Sezione di Ferrara and Dipartimento di Fisica, Università di Ferrara, 44100 Ferrara, Italy

ⁱIstituto Nazionale di Fisica Nucleare, Laboratori Nazionali di Frascati, 00044 Frascati, Italy

^jDepartment of Physics and Astronomy, Ghent University, 9000 Gent, Belgium

^kPhysikalisches Institut, Universität Gießen, 35392 Gießen, Germany

^lSUPA, School of Physics and Astronomy, University of Glasgow, Glasgow G12 8QQ, United Kingdom

^mDepartment of Physics, University of Illinois, Urbana, Illinois 61801-3080, USA

ⁿRandall Laboratory of Physics, University of Michigan, Ann Arbor, Michigan 48109-1040, USA

^oNationaal Instituut voor Kernfysica en Hoge-Energiefysica (NIKHEF), 1009 DB Amsterdam, The Netherlands

^pB. P. Konstantinov Petersburg Nuclear Physics Institute, Gatchina, 188300 Leningrad Region, Russia

^qInstitut for High Energy Physics, Protvino, 142281 Moscow Region, Russia

^rAndrzej Soltan Institute for Nuclear Studies, 00-689 Warsaw, Poland

E-mail: andreas.mussgiller@desy.de, sergey.yaschenko@desy.de

¹Now at: Brookhaven National Laboratory, Upton, New York 11772-5000, USA

²Now at: Siemens AG, 91052 Erlangen, Germany

³Now at: International Atomic Energy Agency, A-1400 Vienna, Austria

⁴Now at: Siemens AG, 91301 Forchheim, Germany

⁵Now at: FAIR Facility for Antiproton and Ion Research, 64291 Darmstadt

⁶Now at: Dept of Radiology, Stanford University, School of Medicine, Stanford, California 94305-5105, USA

⁷Now at: Commonwealth Scientific and Industrial Research Organisation (CSIRO), Australia

⁸Now at: IRCCS Multimedica Holding S.p.a, 20099 Sesto San Giovanni (MI), Italy

⁹Now at: IBA Dosimetry GmbH, 90592 Schwarzenbruck, Germany

¹⁰Now at: Fermi National Accelerator Laboratory, Batavia, Illinois 60510, USA

¹¹Now at: Thomas Jefferson National Accelerator Facility, Newport News, Virginia 23606, USA

ABSTRACT: For the final running period of HERA, a recoil detector was installed at the HERMES experiment to improve measurements of hard exclusive processes in charged-lepton nucleon scattering. Here, deeply virtual Compton scattering is of particular interest as this process provides constraints on generalised parton distributions that give access to the total angular momenta of quarks within the nucleon.

The HERMES recoil detector was designed to improve the selection of exclusive events by a direct measurement of the four-momentum of the recoiling particle. It consisted of three components: two layers of double-sided silicon strip sensors inside the HERA beam vacuum, a two-barrel scintillating fibre tracker, and a photon detector. All sub-detectors were located inside a solenoidal magnetic field with a field strength of 1 T.

The recoil detector was installed in late 2005. After the commissioning of all components was finished in September 2006, it operated stably until the end of data taking at HERA end of June 2007. The present paper gives a brief overview of the physics processes of interest and the general detector design. The recoil detector components, their calibration, the momentum reconstruction of charged particles, and the event selection are described in detail. The paper closes with a summary of the performance of the detection system.

KEYWORDS: dE/dx detectors; Gamma detectors (scintillators, CZT, HPG, HgI etc); Particle tracking detectors; Particle tracking detectors (Solid-state detectors); Detector alignment and calibration methods; Particle identification methods; Data acquisition concepts; Front-end electronics for detector readout.

Contents

1. Introduction	2
2. Detector Design Overview	4
2.1 Design Requirements	4
2.2 General Detector Design	5
3. Detector Components	7
3.1 Magnet	7
3.2 Target Cell	8
3.3 Silicon Strip Detector	8
3.4 Scintillating-Fibre Tracker	11
3.5 Photon Detector	13
4. Data Collection	15
4.1 Data Acquisition System	15
4.2 Performance	17
5. Energy Measurement and Calibration	17
5.1 Silicon Strip Detector	17
5.2 Scintillating-Fibre Tracker	25
5.3 Photon Detector	29
6. Momentum Reconstruction	30
6.1 Spacepoint Reconstruction	31
6.2 Track Finding	32
6.3 Momentum Reconstruction by Coordinate Information	32
6.4 Momentum Reconstruction Using Energy Deposits in the SSD	33
6.5 Alignment	33
7. Detector Performance	36
7.1 Momentum Reconstruction	36
7.2 Particle Identification	37
7.3 Detector Efficiencies	40
8. Event Selection with the Recoil Detector	43
9. Conclusion	46

1. Introduction

In the winter shutdown of 2005/2006 the HERMES spectrometer [1] was upgraded in the target region with a Recoil Detector (RD). The detector surrounded the HERMES target cell and comprised, in a coaxial structure, a set of Silicon Strip Detectors (SSD) situated inside the HERA lepton beam vacuum, a Scintillating-Fibre Tracker (SFT) and a Photon Detector (PD), all surrounded by a superconducting magnet with a field strength of 1 T in the center of the bore. The RD was commissioned during the 2006 data taking and operated in conjunction with the HERMES forward spectrometer until the end of HERA data taking in the middle of 2007.

The purpose of the RD was to improve access to hard exclusive electroproduction of real photons (γ) or mesons (m) off nucleons (N), $e + N \rightarrow e + N + \gamma/m$, at HERMES. Hard exclusive processes have come to the forefront of nucleon structure physics because they provide information on Generalised Parton Distributions (GPDs) [2, 3, 4]. GPDs can be considered the natural complement to transverse-momentum-dependent parton distributions, as both are derived from the same parent Wigner distributions [5, 6]. In particular, GPDs have quickly risen in importance in hadron physics since it was shown that they may provide access to the total angular momentum carried by quarks (and gluons) in the nucleon [7] and they provide a multi-dimensional picture of the nucleon structure [8].

Deeply Virtual Compton Scattering (DVCS), i.e., the hard exclusive electroproduction of a real photon, presently provides the cleanest access to GPDs. GPDs depend on four kinematic variables: t , x , ξ , and Q^2 . The Mandelstam variable $t = (p - p')^2$ is the squared four-momentum transfer to the target nucleon, with p (p') its initial (final) four-momentum. In the ‘infinite’-target-momentum frame, x and ξ are related to the longitudinal momentum of the struck parton, as a fraction of the target momentum. The variable x is the average of the initial and final momentum fractions carried by the parton, and the variable ξ , known as the skewness, is half of their difference. The evolution of GPDs with $Q^2 \equiv -q^2$, where $q = k - k'$ is the difference between the four-momenta of the incident (k) and scattered (k') lepton, can be calculated in the context of perturbative quantum chromodynamics as in the case of parton distribution functions. There exist several GPDs to describe the various possible helicity transitions of the struck quark and of the nucleon as a whole. The DVCS process on an unpolarised proton is very well suited to access the GPD H , which describes the dominant transition that conserves the helicities of both the struck quark and the nucleon.

The DVCS process contributes to the reaction channel $eN \rightarrow eN\gamma$, which is dominated at HERMES kinematics by the Bethe-Heitler (BH) process, i.e., elastic eN scattering with a bremsstrahlung photon in the initial or final state. The two processes are experimentally indistinguishable and therefore interfere. The differential cross section is given by

$$\frac{d\sigma}{dQ^2 dx_B d|t| d\phi} = \frac{x_B e^6}{32(2\pi)^4 Q^4 \sqrt{1 + \epsilon^2}} |\tau_{\text{Total}}|^2, \quad (1.1)$$

where

$$|\tau_{\text{Total}}|^2 = |\tau_{\text{BH}}|^2 + |\tau_{\text{DVCS}}|^2 + \underbrace{\tau_{\text{BH}} \tau_{\text{DVCS}}^* + \tau_{\text{DVCS}} \tau_{\text{BH}}^*}_I. \quad (1.2)$$

In equation 1.1, e is the elementary charge of the electron, x_B is the Bjorken scaling variable $x_B = Q^2/(2pq)$ and $\varepsilon = 2x_B \frac{M}{Q}$ with M the proton mass. The angle ϕ denotes the azimuthal orientation of the photon production plane with respect to the lepton scattering plane. In equation 1.2, the square of the scattering amplitude consists of three parts: one due to the BH contribution, one due to the DVCS contribution and one due to the interference between the two, denoted I . Although the DVCS contribution to the cross section is small at the kinematic conditions of HERMES, it is ‘amplified’ in the interference term I by the (much) larger BH contribution. Experimentally, the preferred way to study DVCS is the measurement of cross-section asymmetries. For an unpolarised hydrogen target, the beam-helicity asymmetry \mathcal{A}_{LU} , where L denotes the longitudinally polarised beam and U the unpolarised target, and the beam-charge asymmetry \mathcal{A}_C can be accessed. These are constructed as

$$\mathcal{A}_{LU}(\phi) = \frac{d\sigma^{\rightarrow}(\phi) - d\sigma^{\leftarrow}(\phi)}{d\sigma^{\rightarrow}(\phi) + d\sigma^{\leftarrow}(\phi)}, \quad (1.3)$$

$$\mathcal{A}_C(\phi) = \frac{d\sigma^{+}(\phi) - d\sigma^{-}(\phi)}{d\sigma^{+}(\phi) + d\sigma^{-}(\phi)}, \quad (1.4)$$

where $d\sigma^{\rightarrow}(\phi)$, $d\sigma^{\leftarrow}(\phi)$, $d\sigma^{+}(\phi)$ and $d\sigma^{-}(\phi)$ represent cross-sections from positive and negative beam helicity and positive and negative beam charges, respectively. Various experimental results on these asymmetries have been published so far by the HERMES collaboration [9, 10, 11, 12]. In these measurements an enriched sample of exclusive events was selected using a missing-mass technique. An event-by-event selection was not possible as the recoiling proton was outside the acceptance and the existing spectrometer did not have sufficient resolution. Monte Carlo (MC) calculations showed that the contribution of events from "associated" production ($ep \rightarrow eN\pi\gamma$, including the resonant production $ep \rightarrow e\Delta^+\gamma$) was expected to be in average 13%, while 3% were expected from semi-inclusive processes. The contribution from the decay products of neutral pions from exclusive reactions that are misidentified as single-photon events was found to be negligible.

The analysis related to the study of DVCS and HERMES employing the RD involves two major motivations. The first is the selection of a DVCS (in the following DVCS corresponds to DVCS and BH) event sample with a background contamination below 1%, and the extraction of a beam-helicity asymmetry from it. This allows a cleaner comparison to predictions from the ongoing theoretical efforts to fit GPD models to HERMES data. The second motivation is the potential to extract an asymmetry in associated production in the Δ -resonance region.

The present paper is structured as follows. Chapters two and three give an overview of the general detector design and the individual detector components. The data acquisition system and the data taking performance are described in chapter four. The energy calibration and the energy measurement in general are outlined in chapter five, and chapter six explains the momentum reconstruction. The performance of the RD is summarized in chapter seven. The event selection with the RD is described in chapter eight. The paper is summarized in chapter nine.

2. Detector Design Overview

2.1 Design Requirements

When using the forward spectrometer alone, exclusivity can only be established for an event sample on a statistical basis due to its limited energy and position resolutions. The purpose of the RD was to provide the necessary information to establish exclusivity on an event-by-event basis and hence reduce the non-exclusive background to below 1%.

The overall design requirements on the RD were defined by the kinematics and type of particles involved in the exclusive reactions of interest and by the expected background processes. The dominant background contribution in the case of DVCS originates from the associated production. Events with higher-mass resonances can be removed by an invariant mass constraint. The particle types to be detected were therefore protons, pions and photons from π^0 decay.

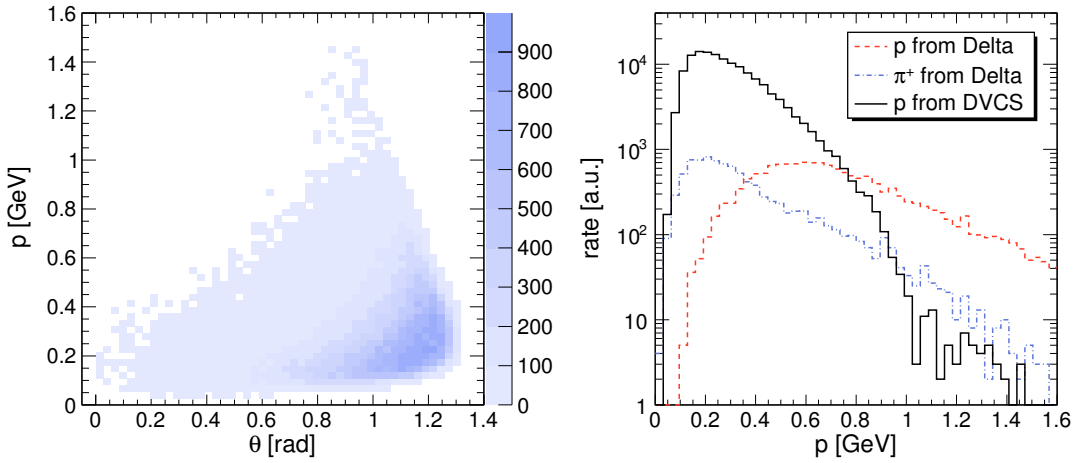


Figure 1. Left: Kinematic distribution of recoiling protons from DVCS in momentum p and polar angle θ in Monte Carlo. Right: Monte Carlo momentum distribution for DVCS recoil protons in comparison with protons and pions from Δ decays.

All exclusive physics processes under investigation at HERMES produce a low-momentum recoil proton at large laboratory polar angles. The left panel of figure 1 shows the kinematic distribution of recoiling protons from MC-generated DVCS events in terms of momentum p and polar angle θ , the angle between the recoiling proton and the beam axis¹. The right panel shows the MC-generated momentum distribution of DVCS protons that were left intact, compared to those of pions and protons from the decay of an intermediate Δ -resonance.

The majority of the recoiling proton statistics is located between 0.5rad and 1.35rad in θ and between 50MeV and 600MeV in momentum. The RD was designed to cover the full θ range and most of the momentum range down to a lower limit of 125MeV, which is imposed by the SSD.

The momenta of particles detected in the forward spectrometer were typically much larger than those of the particle(s) detected by the RD. As a result, the invariant mass resolution was

¹The distributions for exclusive ρ^0 , π^0 and η production look similar.

dominated by the resolution of the forward spectrometer and could not be improved by the RD. However, the transverse momenta of all involved particles were of comparable magnitude. Hence the main exclusivity cuts using the RD can be based on transverse momentum [13]. For this to be effective, the momentum resolution of the RD was required to be better than 10% for momenta below 500 MeV and 15% for higher momenta. In the azimuthal angle ϕ around the beam axis the design resolution was 0.1 rad below 500 MeV and 0.05 rad for higher momenta.

2.2 General Detector Design

The RD consisted of three active detector parts: a silicon strip detector around the target cell inside the HERA lepton beam vacuum, a scintillating-fibre tracker and a photon detector. They were all surrounded by a magnet providing a longitudinal field. The thickness of the target-cell wall was chosen to achieve the lowest possible momentum threshold for the silicon detector. Figure 2 shows a 3-dimensional sectional view of the CAD model of the RD including the target cell and the superconducting magnet. The coordinate system used by HERMES and the RD has the z axis aligned along the beam momentum, the y axis vertical upwards, and the x axis horizontal, pointing towards the outside of the HERA ring. Figure 3 shows a cross-sectional view (in the x-y plane) of all sensitive detector components of the RD including target cell and its support, and the wall of the scattering chamber. These individual components are described in detail in the next chapter. The side view of the HERMES spectrometer together with the RD is shown in figure 4.

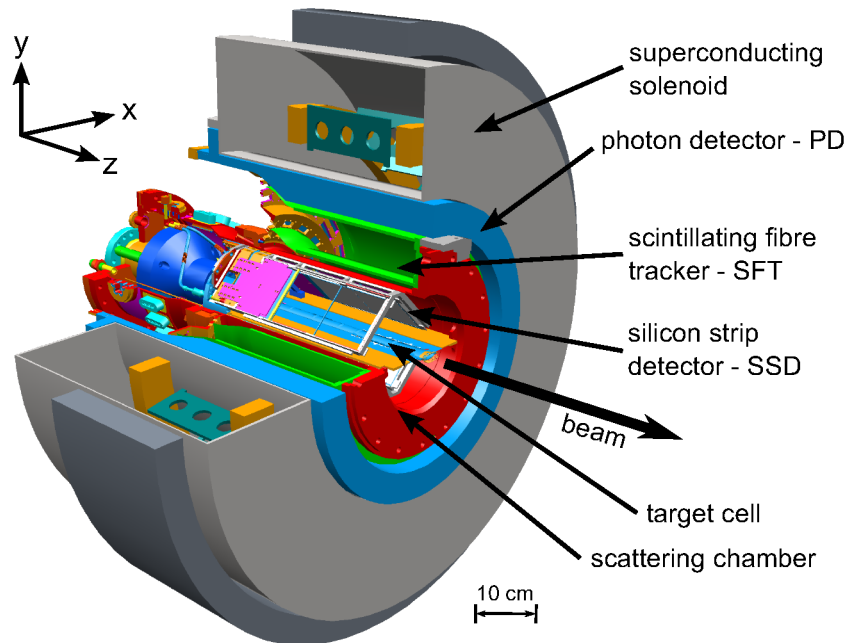


Figure 2. A three-dimensional CAD drawing of the RD.

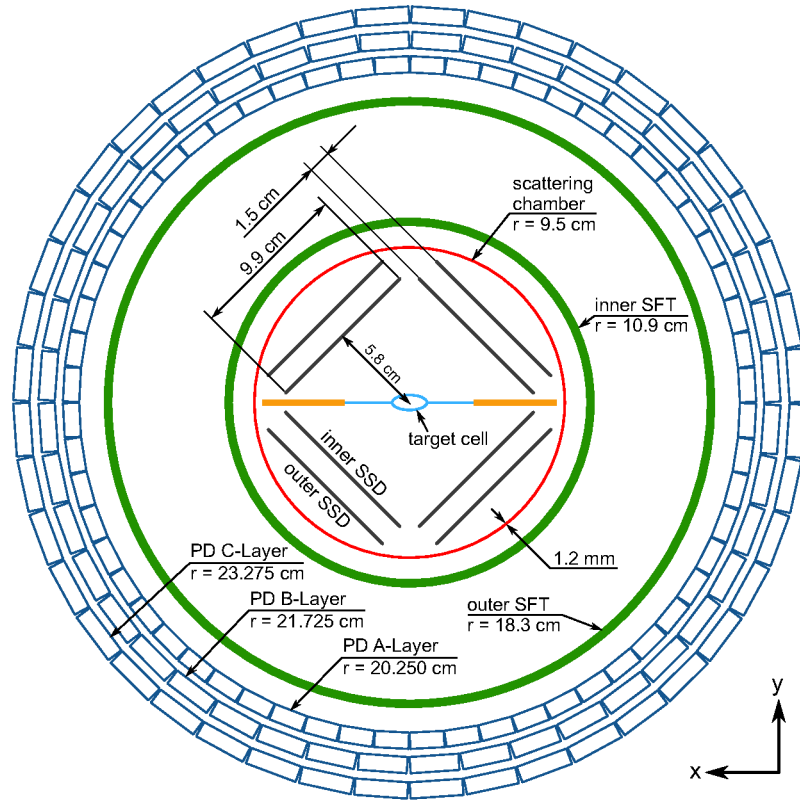


Figure 3. Cross-sectional view of the sensitive detector components of the RD including target cell and its support, and the wall of the scattering chamber. The z axis points into the plane.

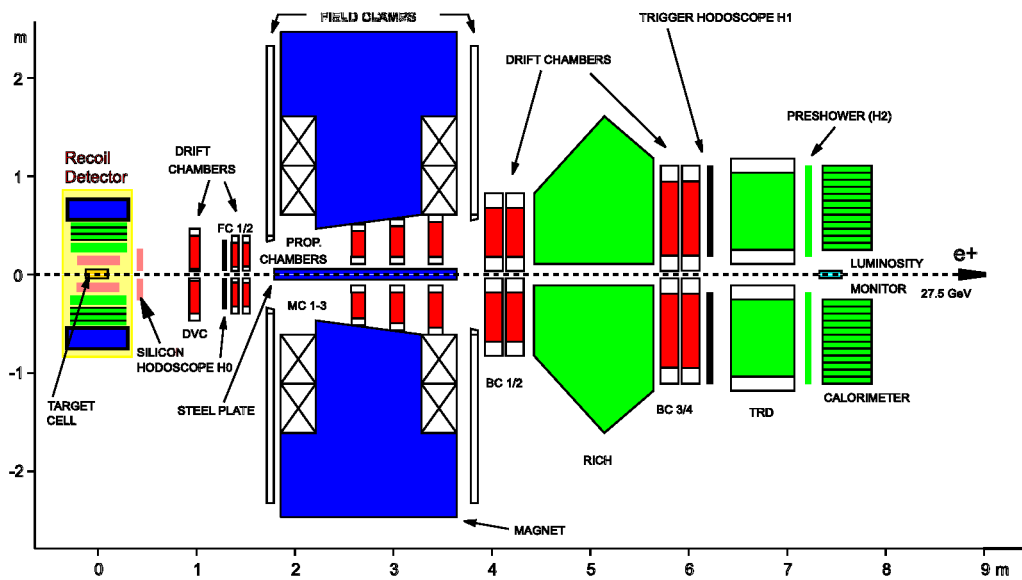


Figure 4. Side view of the HERMES spectrometer with the RD installed in the target region.

3. Detector Components

3.1 Magnet

The active components of the RD were mounted inside the bore of a super-conducting solenoid that provided the field for momentum reconstruction and ensured that Moeller electrons could not reach the SSD. The magnet was built at the D. V. Efremov Scientific Research Institute in St. Petersburg, Russia. The warm bore of the insulation-vacuum vessel of the magnet had a minimum diameter of 501 mm to accommodate the detector. The magnet consisted of two superconducting coils separated by 19.8 cm in a Helmholtz configuration. The coils were made of NbTi wires with a diameter of 0.85 mm and mounted on massive copper rings inside the cryostat. These copper rings provided the necessary mechanical stability for the coils as well as cooling because the coils were by construction only partially immersed in liquid helium. During normal operation, the liquid-helium level was kept at about 80% leaving a small portion of both coils exposed to helium vapor. The operating current was 166 A resulting in a 1 T magnetic field at the center of the bore. The inductance was about 10 H with a stored energy of around 136 kJ in the coils. The quench protection was provided by two large diodes with a critical voltage of 1 V. This limited the ramp-up speed of the magnet to 0.1 A/s. In the event of a quench a maximum voltage difference of 700 V over the coils was observed.

Two concentric heat shields were installed on the inside of the helium vessel as well as on the outside to protect the cryostat from heat radiated off the vacuum vessel. These heat shields were cooled by the cold helium boiling off from the cryostat. RhFe thermal resistors were mounted on both copper rings and on all four heat shields to monitor the temperature of the whole cryostat. For each temperature sensor a three-point calibration was available to determine the actual temperature. Two helium-level probes produced by American Magnetics Inc. were installed in the helium vessel for contingency, each with an active length of 800 mm. The probes ran along the outer surface of the helium vessel in a semi circle. The cryostat was able to hold a maximum of 55 liters of liquid helium. The insulation vacuum was better than 10^{-5} mbar during operation. In order to further protect the magnet from a potential quench due to overheating, cold boil-off helium from the magnet was pumped through the hollow electric leads in order to keep cold the electric terminals, which connected the power supply to the magnet.

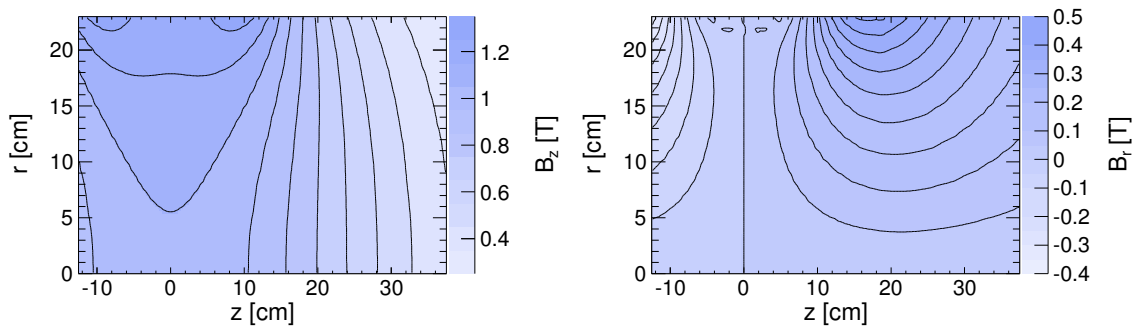


Figure 5. Measured z -component (left) and radial component (right) of the magnetic field as a function of z and radius r .

Prior to installing the magnet in the experiment, the magnetic field was measured in the bore and in the downstream region of the magnet. All three field components were measured simultaneously with three calibrated Hall probes. The step size in each dimension was 1 cm providing an extensive field map for track reconstruction. The z and radial components of the measured magnetic field map are shown in figure 5 with z pointing in the direction of the lepton beam.

3.2 Target Cell

During the period after the RD installation, HERMES exploited both unpolarised hydrogen and deuterium as gaseous targets fed into a storage cell. This target cell consisted of an elliptical aluminium tube installed co-axially to the lepton beam. It had a size of 3 cm (2 cm) in the horizontal (vertical) plane, a wall thickness of $75\ \mu\text{m}$ and an overall length of 25 cm. The gas inlet was located in the longitudinal center of the 15 cm long active length. Up- and downstream of the active length pumping holes covered by a radio frequency shielding mesh were located. The overall position of the target cell was shifted by 12.5 cm downstream with respect to the position of the previously installed 40 cm long cell in order to achieve optimal acceptance of both the HERMES forward spectrometer and the RD (see section 2.1). The upstream and downstream ends of the tube were reinforced with elliptical pieces of aluminium. To the sides, the tube was supported by 4 mm thick aluminium plates. At the upstream end the supports were attached to the scattering chamber, whereas at the downstream end they were supported by two alignment pins.

In order to understand the heating of the cell by the beam, which had a bunch frequency of 10.4 MHz and a bunch length of 28 ps, detailed heating studies on a real target cell were carried out. The studies revealed that a power of approximately 60 W was generated by the beam during a typical HERA lepton beam injection. The target cell was therefore cooled by water flowing through pipes soldered to copper rails running along the support wings on both sides of the cell tube. In order to monitor the temperature of the target cell construction, especially during injection of the HERA lepton beam, two Pt1000 thermal resistors were mounted on the support wings. During regular data collection the temperature measured by both sensors was approximately 16°C which was only slightly above the cooling water temperature, whereas during injection the temperature rose by about 15°C .

3.3 Silicon Strip Detector

The innermost active detector component was the SSD made up of 16 double-sided silicon strip sensors arranged in two layers around the target cell. In order to allow for a minimum detection threshold for protons, the amount of passive material between the interaction point and the first layer of sensors was minimized by placing the silicon sensors and the front-end read-out electronics inside the HERA beam vacuum as close as 5.8 cm to the lepton beam. Each sensor was made of N-type bulk material, and was of the TTT design by Micron Semiconductors Inc. [14]. They had a total area of $99 \times 99\ \text{mm}^2$, an active area of $97.3 \times 97.3\ \text{mm}^2$ and a pitch of $758.2\ \mu\text{m}$. The individual sensor thicknesses varied between $295\ \mu\text{m}$ and $315\ \mu\text{m}$. Two sensors were glued into a holding frame made of Shapal-M [15], which had a thermal expansion coefficient very similar to that of silicon, and combined with the front-end read-out electronics to form a module. Figure 6 shows a sketch of the front and back sides of one module. The strips on the p-side (n-side) of each sensor were oriented parallel (perpendicular) to the HERA lepton beam axis. The signals from the

128 strips on each p- and n-side were routed to the front-end hybrid electronics via $50\mu\text{m}$ thick polyimide foils (flexleads). On the hybrid the signals were split by a charge divider network with a ratio of $\approx 1 : 5$ into a high-gain (HG) and a low-gain (LG) component to increase the dynamic range. For each sensor side, the HG and LG signals were fed to two HELIX 3.0 front-end amplifier chips [16], resulting in eight front-end amplifiers per module. Details on the module and hybrid design can be found in reference [17]. All modules were tested for functionality in a dedicated laser test stand [18]. A full system test in combination with all other RD components was performed prior to the installation at HERMES and is described in reference [19].

In total eight modules were mounted on an aluminium holding structure to build the SSD. In order to minimize the amount of passive material between the inner and outer SSD layers, the inner and outer modules were mounted such that the p-sides, which had less areal coverage by flexleads than the n-sides, faced each other. The distance between the inner and outer SSD layers was 1.5cm and optimized for ϕ resolution while maintaining a high ϕ acceptance taking into account geometrical constraints such as the size of the chosen sensors (including frame), the inner diameter of the scattering chamber, and the thickness of the support structures of the target cell. Under the assumption of perpendicular incidence, the material budget of the SSD was $6.45 \cdot 10^{-3} X_0$ in the area without flexlead coverage and $6.80 \cdot 10^{-3} X_0$ in the area with flexleads. The material budget of the passive material before the inner SSD sensors (target cell wall and n-side flexleads) was $1.02 \cdot 10^{-3} X_0$.

The hybrid was made of a flexible polyimide printed circuit board with a tail that comprised both the signal and supply lines and provided the connection to the vacuum feed-throughs. In addition, the p-side (n-side) hybrids were equipped with a temperature (radiation) sensor. The left

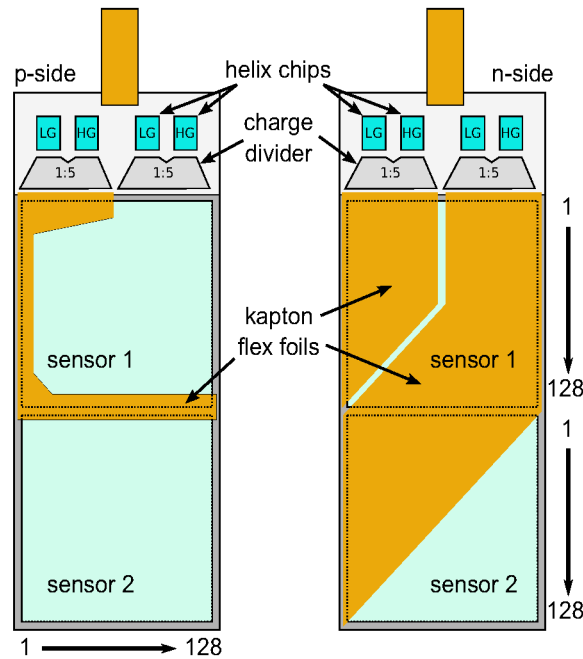


Figure 6. Sketch of the front- and backside of one module of the recoil silicon strip detector (SSD).

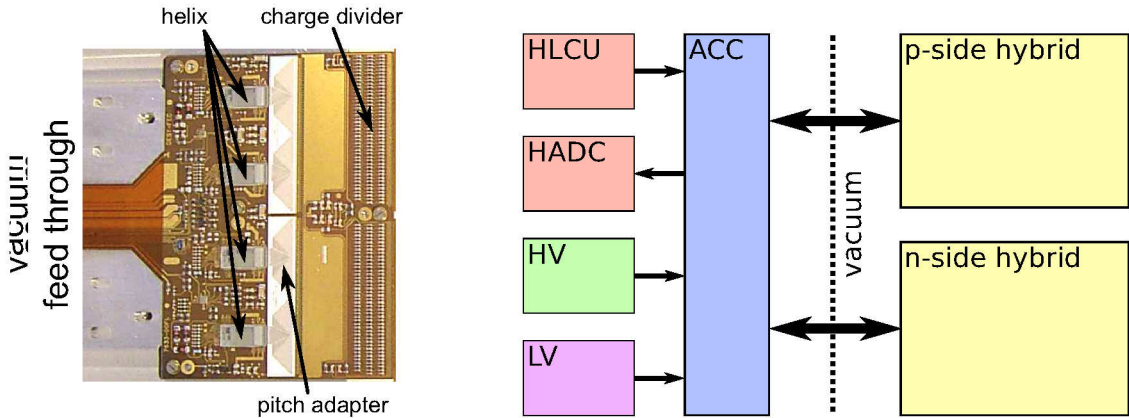


Figure 7. Left: Picture of one of the SSD hybrids. Right: Connection scheme of the hybrids to the read-out electronics (see text for details).

panel of figure 7 shows one of the hybrids with its four HELIX chips, the pitch-adaptor and charge-divider network on the sensor side, and the flexible polyimide tail for the connection. With the front-end electronics operated in vacuum, the hybrids were mounted on a copper heat sink, which was in turn cooled by ethanol at -15°C resulting in a temperature of typically 10°C on the hybrid.

The sketch on the right side of figure 7 shows the simplified connection scheme for the two hybrids of one module (p- and n-sides). The digital control signals required to download setup sequences and control the HELIX chips during read-out were provided by so-called HeLiX Control Units (HLCUs). A single HLCU module was able to serve up to eight daisy chains of HELIX chips. The analog output was digitised by HERMES-ADC modules (HADCs) of which each could handle the data from up to four chains of HELIX chips [20]. The HLCUs and HADC units were produced by ZOT Integrated Manufacturing, Musselburgh, UK. A dedicated Analog Control Card (ACC) was used to merge all signal lines into a single cable per hybrid. The power supply for both the ACC and the connected hybrids was provided by custom made low-voltage (LV) modules, whereas the bias voltage for the sensors originated from commercially available high-voltage (HV) units.

The silicon sensors and the in-vacuum front-end electronics were operated as close as 5.8 cm to the HERA lepton beam under an environment with high transient electromagnetic fields. An elaborate grounding and shielding scheme was therefore developed to avoid radio frequency (RF) pick-up induced by the beam. Figure 8 shows a simplified grounding and shielding scheme. The target cell connected both the up and downstream beam pipes electrically and served as a primary RF shield. The scattering chamber as well as the so-called service chamber, which contained the vacuum feed-throughs for power supply, signals and cooling lines, were connected to the beam pipes. The down-stream end of the scattering chamber was closed by a fine copper mesh with a connection to the beam pipe that shielded the downstream detection systems from radio frequency noise generated in the chamber. The beam pipe, target cell, and service and scattering chambers were all kept at a ground potential common to all HERA beam line components. A cage built around the silicon holding structure acted as a second RF shield (inner shield).

The holding structure was mounted on the scattering chamber with ceramic insulation pieces to electrically decouple the in-vacuum installation from the common HERA ground. In order to

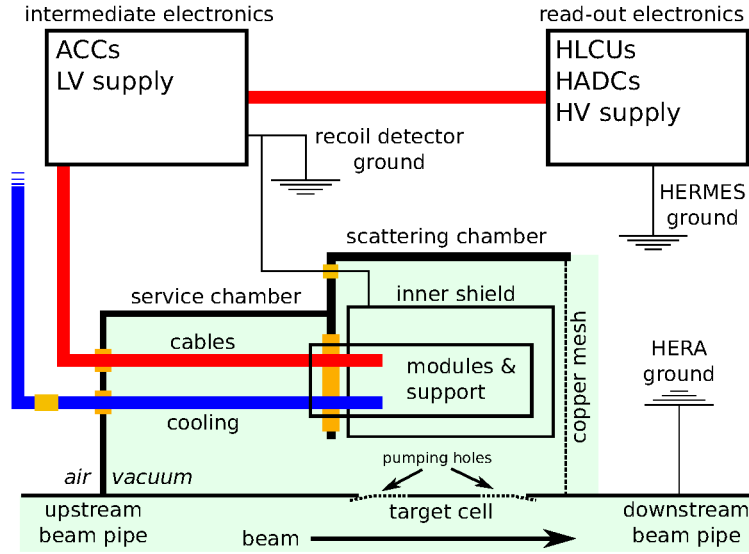


Figure 8. Simplified view of the SSD grounding and shielding scheme. The target cell connects the up and downstream beam pipes and acts as a first shield to avoid radio frequency pick-up. The modules and the holding structures were housed in a cage serving as a secondary shield. The in-vacuum installation was electrically decoupled from the scattering chamber and beam pipe requiring a dedicated RD ground.

decouple the cooling lines from common HERA ground, the vacuum feed-throughs were insulated from the service chamber and additional ceramic insulation pieces were used to break the electrical connection between the in-vacuum cooling lines and the chiller. The intermediate electronics with the ACCs and the LV power supply, located about 3 m away from the interaction region, were kept on a dedicated recoil detector ground, whereas the read-out electronics (HLCUs and HADCs) and the HV supply were kept at a ground potential common to all HERMES read-out electronics components.

3.4 Scintillating-Fibre Tracker

Charged particles with sufficiently large momenta escaped the 1 mm thick aluminium scattering chamber and were detected by the SFT. The SFT consisted of two concentric barrels of scintillating fibres, the inner barrel (SFI) with a radius of about 11.5 cm and the outer barrel (SFO) with a radius of about 18.5 cm. The active length of both barrels was 28 cm. Each barrel in turn was made of two sub-barrels with the inner sub-barrel having the fibres oriented parallel to the beam axis, whereas the corresponding outer sub-barrel had the fibres inclined by 10° (stereo layer). The top two panels in figure 9 show a schematic view of the barrel configuration and the arrangement of fibres in the layers. In both barrels, the two parallel and the two stereo layers (see figure 9 right) can be seen as a single entity, in which for each sub-barrel the outer layer is shifted with respect to the inner one by half a fibre diameter.

The sub-barrels comprised 1318 inner parallel, 1320 inner stereo, 2198 outer parallel and 2180 outer stereo Kuraray SCSF-78M multicladd scintillating fibres with a diameter of 1 mm [21, 22]. In order to form a sub-barrel, modules of 64 (128) fibres for the inner (outer) barrels were joined. Precast moulds with the corresponding curvature and fibre inclination were used in order

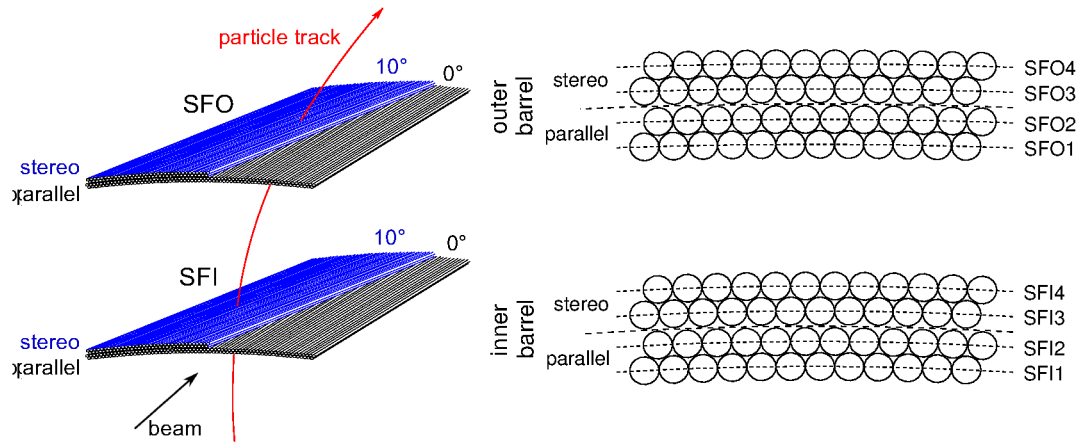


Figure 9. Schematic view of the Scintillating Fibre Tracker (SFT) barrel configuration (left) and the arrangement of fibres in the layers (right).

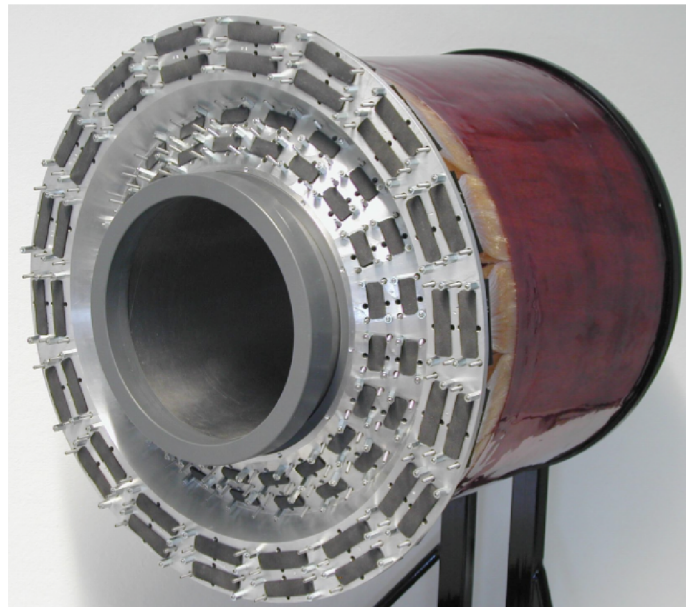


Figure 10. Picture of the assembled SFT mounted over a mockup scattering chamber.

to produce the four different types of modules used in the SFT. The far-end faces of the fibres were metallised, leading to an increase in light yield by 20%. The near ends were glued into custom made connectors mounted on an aluminium holding structure. Figure 10 shows the assembled SFT mounted on a dummy scattering chamber. The connectors at different radii on the upstream holding ring are visible at the left side of the picture, indicating the four sub-barrels. The produced scintillation light from each module was fed to 78 64-channel Hamamatsu H7546B Multi-Anode PhotoMultiplier Tubes (MAPMTs) [23] via 4m long light guides made of Kuraray clear fibres. Besides the space constraint, also the sensitivity of the MAPMTs to magnetic field was a reason

for placing the MAPMTs at a distance of 2.5 m from the magnet z-axis. With additional μ -metal and soft-iron shielding the maximum field at the location of the MAPMTs was reduced to 5 mT.

In the inner barrel, 32 fibres from a regular layer and the corresponding shifted layer shared one MAPMT, with one fibre connected to one MAPMT pixel, whereas for the modules in the outer SFT barrel two fibres, one from the regular and one from the shifted layer, were joined in the connector on the MAPMT end of the light guides. In order to allow for a distinction between cross-talk on the MAPMT surface and cross-talk between neighbouring active fibres, neighbouring active fibres were not connected to neighbouring pixels on the MAPMT but rather in a more elaborate scheme (see section 5.2). The MAPMT has its 64 channels arranged in a 8×8 grid of $2 \times 2 \text{ mm}^2$ pixels and provides a high-speed response while having low internal cross-talk despite the high integration of electronics components. In addition to the 13 dynode stages for each pixel, the MAPMT provides a common signal for all pixels after the 12th stage (denoted as dynode-12 signal). All MAPMTs were tested prior to installation [24].

The readout electronics for the MAPMTs were based on the design of the HADES-RICH Preprocessing Front-end Module (PFM) [25] with an additional charge-divider network between the MAPMTs and the PFMs to adjust the signal amplitudes. This readout system allowed to obtain information on the energy deposit, which is exploited in the particle-identification procedure (see section 7.2). The readout system had an integration time of about 600 ns, which meant that the signals from 7 HERA lepton-beam bunches were summed for each MAPMT channel. In order to avoid the combination of hits from different bunches reconstructed into a single track, the dynode-12 signal was read out by a fast commercially available multi-hit Time-to-Digital Converter (TDC).

3.5 Photon Detector

The main purpose of the outermost active detector component, the PD, was the detection of photons, however, it was also capable of detecting pions and protons with momenta above approximately 300 MeV and 500 MeV, respectively. In order to obtain good photon-detection efficiency, and taking into account geometric constraints, the PD was built as a cylindrical volume of three subsequent layers of alternating tungsten as a converter and plastic scintillator material for the detection of the charged (shower) particles.

The layer thickness of the photon detector was optimized based on Monte Carlo simulation. The innermost tungsten layer was 6 mm thick, whereas the two following tungsten layers were each 3 mm thick. This corresponded to a total thickness of 3.4 radiation lengths, and resulted in a 85% photon-conversion probability at the characteristic photon energies of about 150 MeV.

The plastic scintillator material was BC-408 from the manufacturer Saint-Gobain Corporation [26]. Each scintillator layer of the PD was segmented into strips. The inner layer (*A* layer) had 60 strips, which had a trapezoidal cross section for maximal coverage. The strips were 27.5 cm long, 1 cm thick and had a mean width of 2.05 cm. They were arranged parallel with respect to the beam line. The subsequent stereo layers had 44 strips oriented under an angle of $+45.6^\circ$ for the second layer (*B* layer) and -46.2° for the third layer (*C* layer) in order to allow for a spatial reconstruction of the photons. The overlap between a parallel and a stereo layer resulted in a polar-angular resolution of about 2.7° . The stereo strips were fabricated out of rectangular straight blocks of 1.00×2.10 (1.00×2.25) cm^2 for the second (third) layer, then bent, twisted and cut into their final shape. This resulted in an effective cross section in the plane orthogonal to the beam axis

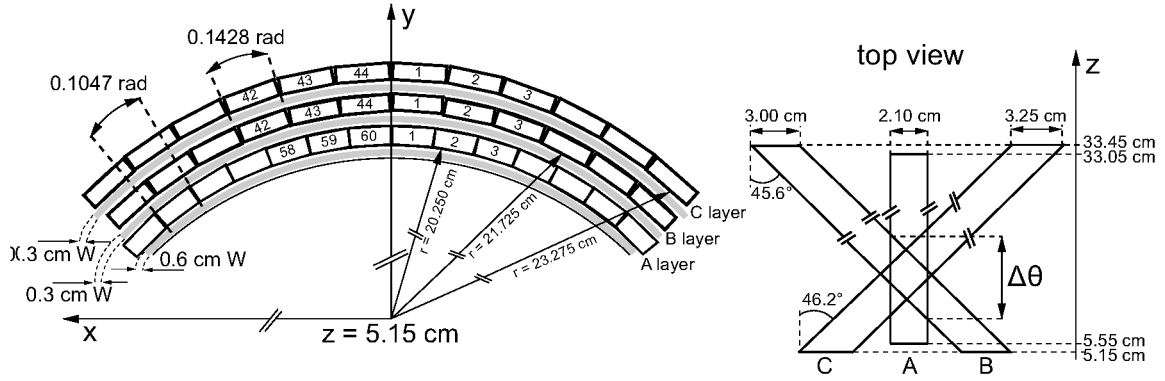


Figure 11. Geometric description of the PD in the HERMES coordinate frame. The strip numbering is also indicated. For clarity, the picture is not to scale.

of 1.00×3.00 (1.00×3.25) cm^2 . The strips covered a length of 28.3 cm along the beam line. A schematic drawing of the PD is depicted in figure 11.

Two 60 cm long round wavelength-shifting fibres with a diameter of 1.5 mm were glued with BC-600 optical cement in grooves along each side of a strip to capture and redirect the scintillation light from the strips to 2 m long clear light guides. The fibres (clear light guides) were BCF-91A (BCF-98) from the same manufacturer as the scintillator strips. In order to increase the light yield, the strips were covered with BC-620 reflective paint and the wavelength-shifting fibres were mirror coated at their extremity.

Figure 12 shows a picture of the PD during construction. Clearly visible are the white-painted strips of the outermost layer, which are oriented under a stereo angle. The wavelength-shifting fibres, with their green light output, were connected to optical connectors. In the picture the excess ends of the fibres point straight up. Not shown are the clear light guides that are connected to the depicted optical connectors. In the final assembly, care was taken to ensure that the detector was completely light tight by covering it with black foil and black paint.

The readout of the clear light guides was performed by 6 Hamamatsu 64-channel H7546B multi-anode PMTs (MAPMTs) [23]. The cathode pixel size was $2 \times 2 \text{ mm}^2$, which allowed for the connection of one fibre per pixel. In order to minimize influence of cross-talk on the MAPMT cathode, the arrangement of the light guides on the MAPMT pixel matrix followed a scheme similar to that of the SFT. The MAPMTs were, each individually, surrounded by two 0.2 mm thick μ -metal sheets and placed in a soft-steel case of 14 mm thickness [24]. Per group of three they were then placed in an additional soft-steel box. The boxes were installed at a distance of 1.5 m from the magnet, where the magnetic field was of the order of 20 mT, which was reduced to 0.2 mT inside the shielding.

The signals from the MAPMTs were transferred to a patch panel, and from there to the transmitter electronics. In the transmitter, signals originating from the same strip were summed together, amplified, and transported as a differential signal over 30 m long flat cables to the receiver electronics. The receiver converted the signals back to non-differential signals, amplified them, and sent them over 70 m of flat cable, acting as a time delay, to 6 charge-integrating analog-to-digital converters (ADCs), one per MAPMT. Also here, to allow for cross-talk correction, care was taken that



Figure 12. Picture of the PD during its assembly.

channels adjacent in the flat cables were neither neighbouring pixels on the MAPMT surface nor adjacent strips in a PD layer.

Although the time between two HERA bunches amounted to 96 ns, the gate width for the readout of the ADCs was set to 250 ns in order to accommodate the full length of the PD signals. According to test measurements performed during commissioning no signal overlay was observed.

4. Data Collection

4.1 Data Acquisition System

The integration of the RD into the HERMES data-taking infrastructure [1] involved the additional readout of 8192 channels for the SSD, 5120 channels for the SFT and 192 channels for the PD.

The original HERMES Data Acquisition (DAQ) system was built using Fastbus crates with crate controllers based on the now outdated Motorola M68020 microprocessor and two Digital Signal Processors (DSPs). Already at the time of the RD upgrade planning, these modules were not easily available on the market. Programs for microprocessors and DSPs for each particular crate were written in assembler language and had substantial volume and complicated structure. All this made extending the existing system by adding identical readout equipment for the new detectors unreasonable. Instead, another approach was chosen.

The basic concept of incorporating the RD readout into the HERMES DAQ was the preservation of the existing hardware and software structure, i.e., building an event online in contrast to

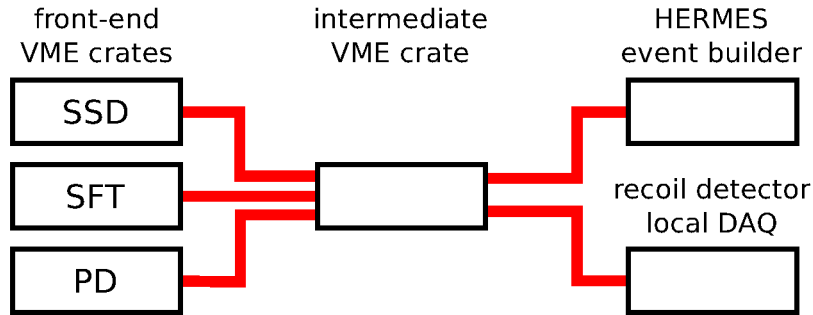


Figure 13. Schematic diagram of the RD data acquisition system. The digitisation devices for each sub-detector were housed in separate front-end VME crates. These crates were connected via optical links to a so-called intermediate VME crate that managed the connection of the front-end crates with either the HERMES event builder or the local RD DAQ.

merging two independent data streams offline. The benefits of such an approach were minimal software changes in the offline data processing and online monitoring. The only modifications to the software involved the inclusion of new data streams into the online event reconstruction and the addition of proper decoding and reconstruction in the offline software chain. Another important aspect of the upgrade was the use of modern and readily available components, like PCI-VME (Peripheral Component Interconnect - Versa Module Eurocard) bus controllers with onboard DSPs. The final readout system, schematically shown in figure 13, consisted of three VME crates with DSP-based controllers assigned to each individual sub-detector. The front-end electronics consisted of HADC modules for the SSD, TDCs and custom-made Readout Controllers (RC) for the SFT, and charge-to-digital converters for the PD. The controllers were connected via optical links to intermediate VME interfaces located in a fourth auxiliary crate. This crate also hosted both intermediate VME controllers for the two independent readout chains. One of these was connected to the main HERMES event-builder DSP, responsible for reading data from all crate controllers and assembling the final event structure. The second VME controller was connected via an optical link to a PCI controller in a PC dedicated to service tasks on all sub-detectors of the RD. This control structure allowed the use of the old and new detector components in parallel and independently of each other. It was, for example, possible to take data with the HERMES forward spectrometer without RD and, at the same time, perform test and calibration runs using stand-alone programs on the dedicated PC. In order to switch between this and HERMES full data-taking mode, including the RD, the required action was minimized to reloading the DSPs and changing the trigger dead-time logic [27].

In addition to the readout of the main event content, a system for status and control information was provided. It included the readout of temperature and radiation sensors for all modules of the SSD, temperature sensors on the target cell and status information of the SSD cooling system. This so-called slow control information was read out in 10 second intervals.

During data taking, the trigger for the readout of the RD was provided by the HERMES spectrometer. For dedicated pedestal and calibration runs a random trigger was used. For recording cosmic ray muons, a signal in the lower half or a coincidence of a signal in the upper and lower halves of the PD was used to trigger the RD read-out.

4.2 Performance

Data were collected in 'runs' which had a size of 500 Megabyte of raw data originating from all sub-detectors of HERMES. Under regular data taking conditions and with all sub-detectors active (including RD) a single run comprised of the order of 25000 events. Collection of data including the RD started in February 2006 with a commissioning phase in order to set up and tune all RD components.

At the end of February 2006, during a HERA lepton beam injection, beam-induced radio frequency (RF) was the most probable cause of over-heating of the target-cell foil, which resulted in a hole in the foil of about 1 cm^2 in size. The opening in the primary SSD radio frequency shield allowed RF to escape. This caused in turn the SSD to stop operating properly and meant also a substantial delay in the commissioning. Only after a second RF incident during injection and the repair, exchange and repositioning of several modules of the SSD, the commissioning could continue and was successfully finished end of September 2006. During the final installation, the flat cable connecting the n-side hybrid of one module to the vacuum feed-through broke and caused this module side to become unusable. Of the 91000 runs collected in the years 2006 and 2007, 69% were collected with fully commissioned SSD of which 4.7% runs were marked as having one or more non-working HELIX chips. This state was mainly caused by read-out chips losing their programming, which was typically quickly recognized by the shift crew and resolved by reprogramming. The overall data-taking efficiency of the SSD in the time after final commissioning was 90%.

In the case of the SFT, the overall data taking performance was 96%. Runs were labeled as bad due to either desynchronisation of the SFT readout system with respect to the HERMES DAQ or due to data corruption. Both effects were automatically cured by reinitialisation of the SFT readout system at the beginning of each run.

The PD had a data-taking efficiency of 99.6% during the data taking period with all sub-detectors commissioned and fully operational.

5. Energy Measurement and Calibration

5.1 Silicon Strip Detector

In order to improve the reconstruction of the momentum of protons, the energy deposits in both SSD layers are used as additional measurements. For good performance a precise energy measurement is thus essential.

An initial energy calibration was performed at the Tandem Accelerator of the University of Erlangen as described in reference [28]. Each module was mounted on a movable carrier inside a vacuum chamber and each strip was irradiated with protons of 3.5, 4.0 and 9.0 MeV kinetic energy. This allowed for a determination of the ratio between high and low gain channels, the cross-talk behavior as well as an absolute energy calibration. However, as the environmental conditions at the final installation at HERA were extremely different compared to the ones present during the calibration, the obtained coefficients could not be used during data taking and the analysis. The subsequent sections describe the steps necessary for a precise determination of the energy deposit and energy calibration based on data collected during detector operation.

Raw-Data Corrections

In order to achieve the required resolution and absolute precision, several corrections on the raw data must be applied. They are described in the following paragraphs.

Pedestal Stability During data taking, every 2 – 3 hours dedicated pedestal data were collected. The panels of figure 14 show the mean value of the pedestal for three selected channels for about two months worth of collected pedestal data. The channel indicated by the triangles (boxes) shows medium (large) fluctuations, whereas the channel indicated by the circles only shows a slow drift over time. In figure 15 the same pedestal data are displayed versus the beam current at which the pedestal run was taken, using the position of the pedestal obtained from the most recent pedestal run without beam as an absolute reference. For the channels indicated by triangles and boxes a clear dependence of the pedestal position on the beam current is visible. A behavior that resulted in a drift of more than one ADC channel during a typical HERA fill with a beam current of ≥ 25 mA was shown by 25% of the low gain and 79% of the high gain channels, randomly distributed throughout the SSD.

For both the high and the low gain channel of each strip a quadratic parameterisation of the beam-current dependence was used to correct for the drift of the pedestals between two pedestal runs. The parameterisations gave an offset based on the change of the beam current between the last pedestal run and the analysed event. This offset was added to the raw data to correct for the drift.

Correlated Noise The HADC used to digitise the data delivered by the HELIX chips performed an online common-mode correction, i.e., the correction for a common shift of the signal base-line, based on the data from the first 16 non-hit channels out of the first 32 channels of each chip. For pure common-mode noise this implementation is sufficient. However, the data contain additional correlated noise that cannot be corrected for by this common-mode correction algorithm.

The left panel of figure 16 shows the ADC value for the 128 channels of a chip after pedestal subtraction and common-mode correction performed by the ADC. The common-mode correction performed well in the beginning of a chip (up to approximately channel 20). Beyond this region,

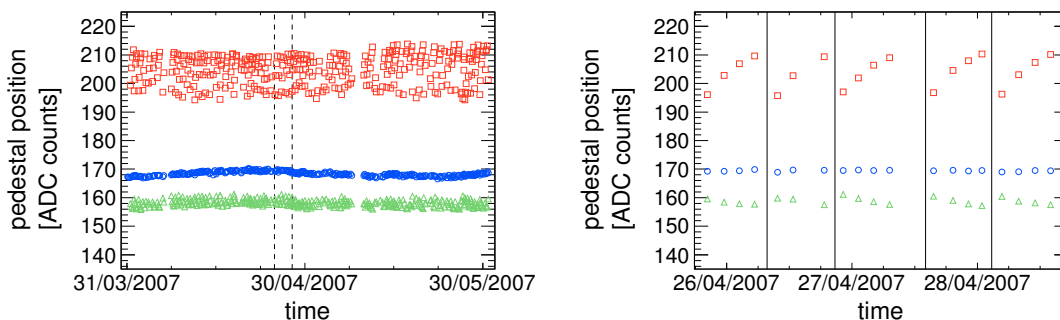


Figure 14. Left: Measured pedestal position for three selected channels versus time for about two months of collected pedestal data. Right: A zoom into the period indicated by the dashed lines in the panel on the left showing the pedestal data for five consecutive HERA fills.

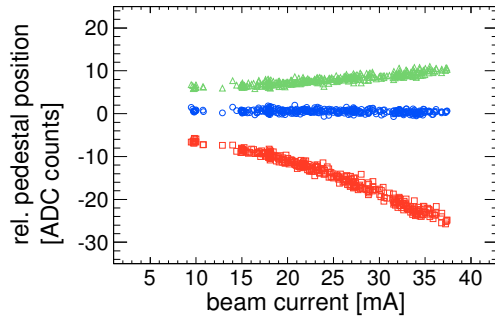


Figure 15. The same pedestal data as in the previous figure displayed versus the beam current at which the data were collected. The pedestal data collected without beam is used as an absolute reference. The graphs are shifted by 5 ADC counts with respect to each other for better visibility.

the width of the pedestal increased with increasing channel number. In the right panel of figure 16 the ADC values of all channels of a chip versus channel number are shown for a single event. At around channel 100 one can observe an actual charge signal with an amplitude of 100 ADC counts. However, a substantial offset is present, as the baseline for this particular event drifts towards positive ADC values for increasing channel numbers.

In order to correct for the drift, the data from every eighth channel (starting from channel 28) of each chip were always read out and used as base points for a spline interpolation. In the right panel of figure 16, the base points are indicated by square markers. The actual spline is shown as a line through the base points. The result from the interpolation was used to correct for the drift. In the case that the signal of a spline-interpolation base point after common mode correction is above a certain threshold and hence part of an actual cluster, the average signal of the two neighbouring base points is used in the interpolation.

In the right panel of figure 17, the same event is shown after the spline-interpolation correction.

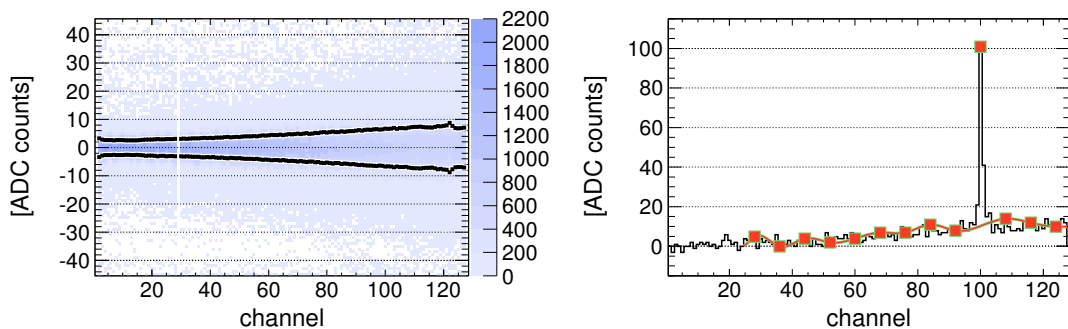


Figure 16. Left: Pedestal ADC spectrum for all channels of a chip versus channel number after pedestal subtraction and common-mode correction in the ADC. The lines in the figure indicate the $\pm 1\sigma$ band of the pedestal width. The blank vertical band close to channel 30 is caused by a non-working channel. Right: Data after pedestal subtraction and common-mode correction for a single event. The markers indicate the channels used for the correlated noise correction with a spline interpolation shown as dashed line. The data was taken without zero-suppression.

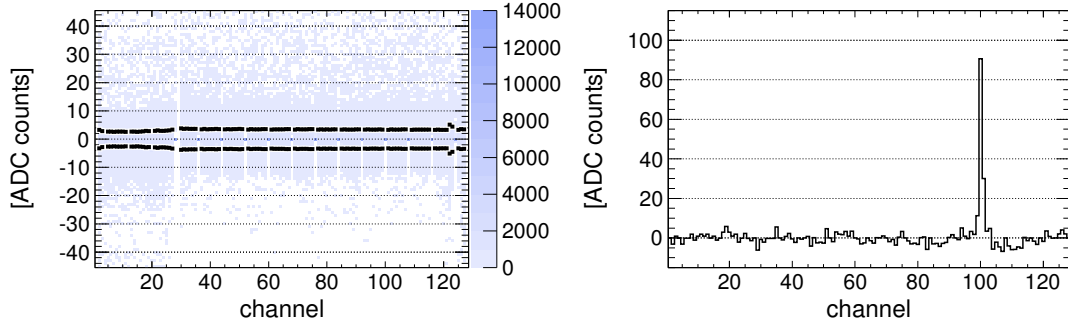


Figure 17. Left: Pedestal ADC spectrum for all channels of a chip versus channel number after the correction for the correlated noise. The lines in the figure indicate the $\pm 1\sigma$ band of the pedestal width. The blank vertical band close to channel 30 is caused by a non-working channel. Right: Data for the sample event from the previous figure after correction for the correlated noise.

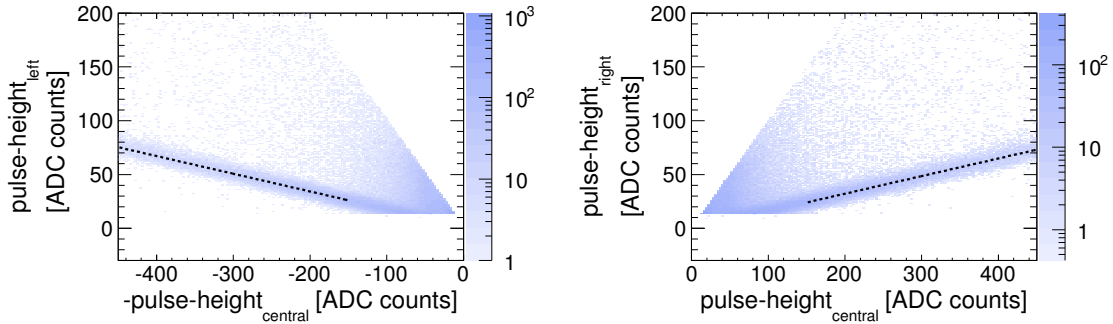


Figure 18. ADC value of the channel to the left/right of the channel with the highest ADC value in a cluster (central channel) versus the ADC value of the central channel before cross-talk correction.

The baseline over the full chip is flat and the amplitude of the hit at channel 100 is reduced to approximately 90 ADC counts. For a larger data sample, the spline-interpolation corrected ADC values versus channel number are shown in the left panel of figure 17. Again, the lines indicate the $\pm 1\sigma$ band of the pedestal width. After the correction, the pedestal width is below 3 to 4 ADC counts over the full sensor side. A detailed description of the method including results from systematic studies can be found in reference [29].

Cross-talk For each actual signal in a channel a significant fraction of that signal migrates into the neighbouring channels. This cross-talk is due to coupling between strips on the sensor, the traces on the flex foils and the chip itself. Figure 18 shows the ADC value of neighbouring channels as a function of the ADC value of the central channel of a cluster with central channel denoting the channel with the highest ADC value. Both to the left and to the right a band indicated by dashed lines is seen. The slopes of the bands correspond to the constant fraction of signal that migrates to the neighbours. The cross-talk to the left neighbour was between 11% and 16%, whereas to the right it was between 15% and 21%. In addition, the cross-talk is different for even and odd numbered strips which can be explained by the internal design of the HELIX chip.

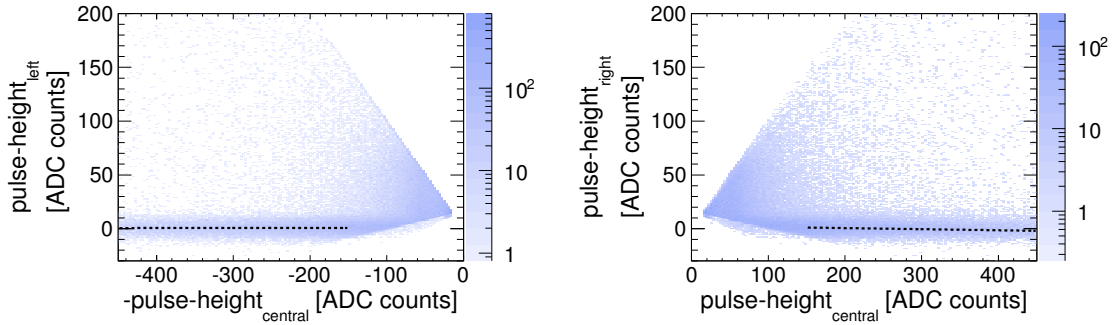


Figure 19. ADC value of the channel to the left/right of the channel with the highest ADC value in a cluster (central channel) versus the ADC value of the central channel after cross-talk correction.

The left-right asymmetry in the cross-talk would introduce a bias in the position measurement in the silicon sensor and therefore needs to be corrected for. In addition, the cross-talk correction is capable of recovering signals below the hardware threshold. The algorithm assumes that the 128 uncorrected ADC values originate from a 128×128 matrix multiplied by the 128 actual ADC values. The matrix elements represent the fractions of signal migrating into other channels, i.e., the fraction of signal remaining in a channel is represented by the diagonal elements and the cross-talk to neighbouring channels by the off-diagonal elements. The cross-talk to the second neighbour is of the order of 2%. Cross-talk effects to channels farther away from the central channel are insignificant and therefore neglected in the correction. By matrix inversion² it is possible to reconstruct the actual ADC values. Figure 19 shows the ADC values of the left and the right neighbour versus the ADC value in the central channel after the cross-talk correction. After the correction the bands are horizontal and have a mean around zero. A detailed description of the SSD cross-talk correction can be found in reference [30].

High-Low Gain Relation

For each strip the cross-talk corrected ADC values for both high-gain and low-gain channels are combined to an effective low-gain ADC value. In the left panel of figure 20, the ADC values of the high-gain channel are plotted versus the ADC values of the low-gain channel, for all 128 strips of one sensor side. The figure shows a linear behavior with a slope of ≈ 4.3 up to ≈ 500 ADC counts for all 128 high-gain channels after which they reach their individual saturation levels. For each individual strip the relation between both channels is extracted by a fit of a second-order polynomial to the data. A quadratic polynomial with the offset fixed at zero is chosen to account for non-linearities of individual strips not visible in the integral distribution shown in the left panel of figure 20. For ADC values below the saturation level in the high-gain channel, the effective ADC value is calculated from the high-gain value, whereas for ADC values above the saturation level in the high-gain channel it is simply the low-gain ADC value.

²The correction algorithm assumes that cross-talk affects only the immediate and second neighbours to the left and right of the central channel. It is therefore sufficient to invert a 5×5 submatrix to perform the correction.

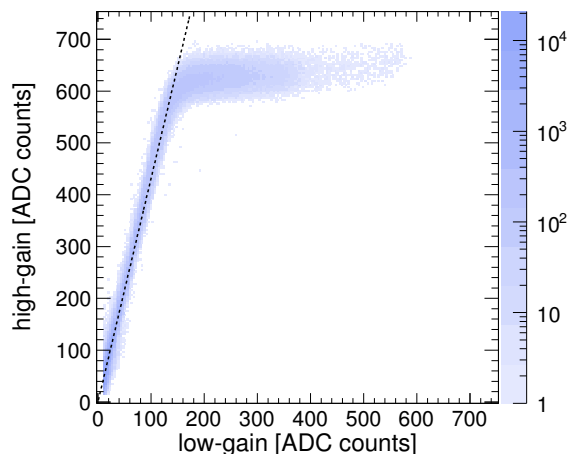


Figure 20. ADC values of the high-gain versus those of the low-gain channel for all 128 strips of a sensor side.

Clustering

A cluster is formed by combining adjacent strips that have a real signal. A new cluster is created in the case that the signal of a strip is above a threshold corresponding to 60 keV energy deposit. Neighboring strips are added to the cluster if their signal is above a secondary threshold corresponding to 50 keV. The amplitude (position) of a cluster is calculated as the sum (barycenter) of energy deposit values of all strips in the cluster.

Absolute Energy Calibration

For protons stopped in the outer SSD layer as well as for protons with too low momentum to reach the SFT layers, the momentum is reconstructed using just the energy deposits in both SSD layers. In this momentum region the quality of the momentum reconstruction is therefore directly related to the precision of the energy calibration. In the first iteration, the energy calibration is obtained via the energy deposits for protons and deuterons that are stopped in the outer SSD layer and for protons that punch through this layer. The left panel of figure 21 shows the energy deposit in the inner SSD layer versus the energy deposit in the corresponding outer SSD layer after a correction for the incident angle. The curves in the panels show the results of a Geant4 simulation [31, 32] with protons that penetrate the sensors under an angle of 90° , i. e., they represent the theoretical energy deposit. At a momentum of about 125 MeV, a proton has sufficient energy to punch through the inner SSD layer and reach the outer layer where it is stopped. For momenta above approximately 145 MeV protons also punch through the outer layer.

The comparison of the distribution shown in the left panel of figure 21 with the theoretical values is used to obtain the absolute energy calibration for all sensor sides. This is shown in the right panel of figure 21 in which the most probable values of a Landau distribution convoluted with a Gaussian, obtained from fits to the distribution of energy deposits in the inner SSD layer versus the energy deposit in the outer SSD layer, are presented. The fit results for each combination of an energy deposit measured on one side of an inner sensor with an energy deposit measured on one

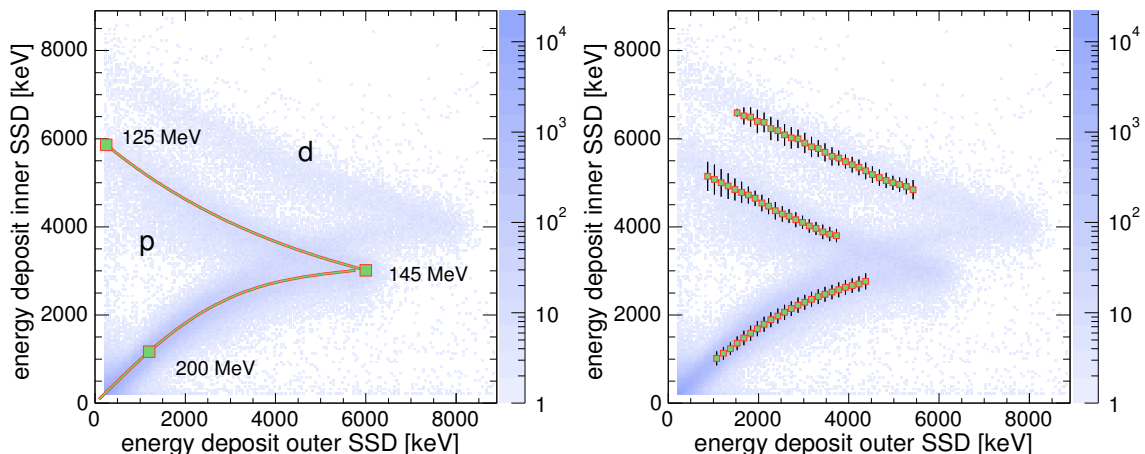


Figure 21. Left: Energy deposit in an inner SSD sensor versus the energy deposit in the corresponding outer SSD sensor obtained from data taken with the deuterium target using preliminary calibration constants. The solid curve represents the most probable energy deposit and the markers the corresponding momentum of protons. At a momentum of 125 MeV protons have sufficiently high momentum to reach the second layer of the SSD where they are stopped up to a momentum of 145 MeV. The second band originates from deuterons being stopped in the second SSD layer. Right: The same data with markers indicating the most probable energy deposits of protons and deuterons stopped in the outer layer and protons that punch through the outer layer as obtained from fits to the distribution.

side of an outer SSD sensor are then used in a combined fit to the theoretical curves. The overlap between the proton and deuteron bands for particles passing through both SSD layers could lead to a bias in the absolute energy calibration, which is taken into account by assigning lower weights to these data points in the combined fitting procedure. The procedure is shown in figure 22 for one specific combination of inner and outer sensors. The deviation between the measured data and the theoretical energy deposition clearly indicates a non-linear detector response. In order to compensate for this non-linearity the energy deposits of clusters in the inner and outer layers are expressed by

$$\Delta E_{\text{inner}} = f(ADC_{\text{inner}}^{\text{cluster}}) \quad \text{and} \quad \Delta E_{\text{outer}} = f(ADC_{\text{outer}}^{\text{cluster}}), \quad (5.1)$$

respectively, where ADC^{cluster} are the sums of ADC values in a cluster, ΔE are the calibrated energy deposits and f is a function of four parameters describing two connected polynomials. The function is constructed such that there is a smooth transition at the connection point and that the behavior is quadratic (linear) for ADC^{cluster} values below (above) the connection point. In this way, non-linearities in the region of low ADC^{cluster} values can be corrected, while there is still stable behavior for large values of ADC^{cluster} .

The final 16 calibration coefficients for the combination of both p- and n-sides of one inner and one outer sensor are obtained by a combined minimization of the differences between the measured band positions (crosses) and the theoretical curves shown in all panels of figure 22. The results of the calibration procedure applied to the uncalibrated data points is shown as open boxes in the panels demonstrating a good agreement of the calibrated data points with the expected curves.

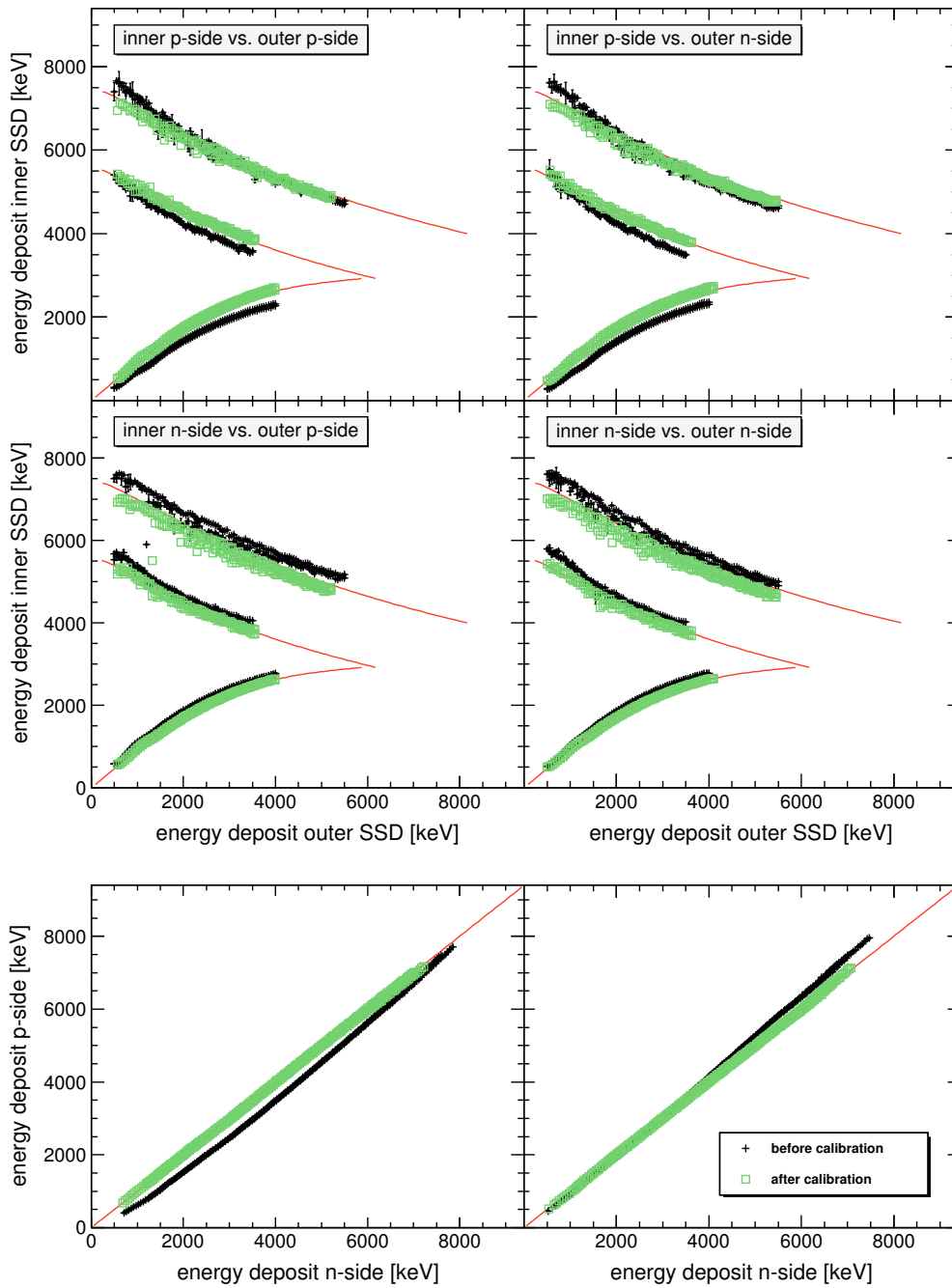


Figure 22. Top: Energy deposit in an inner sensor versus the energy deposit in the corresponding outer sensor for all combinations of p- and n-side energy deposit measurements. Bottom: Energy deposit measured by the p-side versus energy deposit measured by the n-side for an inner and the corresponding outer SSD sensor. In all six panels, the curves represent the theoretical values taking the individual sensor thicknesses into account. The crosses show the data before calibration whereas the open boxes depict the same data after calibration.

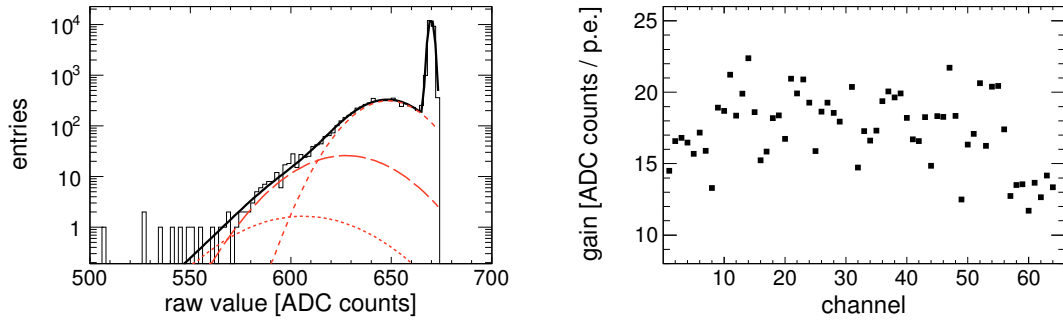


Figure 23. Left: Raw ADC amplitude spectrum for a single MAPMT pixel obtained by flashing the surface of the MAPMT with blue light. The position of the pedestal peak (at the right of the spectrum) is obtained from a fit to the distribution. The spectrum is inverted due to the readout logic of the used PFM. Right: Gain expressed as ADC counts per photoelectron for all 64 channels of one MAPMT.

5.2 Scintillating-Fibre Tracker

Although the main purpose of the SFT was to provide position information for the reconstruction of charged tracks, the measured energy deposits are also valuable quantities that are used in the particle-identification procedure. In contrast to the SSD, this requires only a relative energy calibration. For the SFT, the conversion from ADC values to energy deposits is performed in two stages. In the first stage, the raw ADC values are converted to the number of photoelectrons seen by a MAPMT pixel. The second stage is the conversion from the number of photoelectrons to an actual energy deposit. As mentioned before, cross-talk is assumed to originate from neighbouring fibres or neighbouring pixels on the MAPMT. The correction is therefore performed in units of photoelectrons.

PMT Gain Calibration

The gain of the Hamamatsu MAPMT is of the order of $10^5 - 10^6$ for supply voltages between 800 V and 1000 V. In order to calibrate the response of the MAPMT pixels in terms of photoelectrons, each pixel was illuminated with blue light originating from a LED [33] and the data were acquired with the same read-out system as used in the final SFT installation. The obtained distributions were

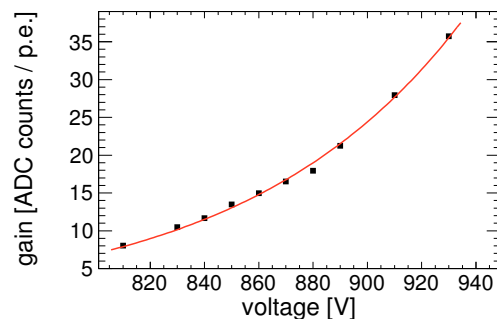


Figure 24. Dependence of the MAPMT gain on the applied supply voltage.

fitted with a function describing both the pedestal peak and the signal contributions from 1, 2, and 3 photoelectrons. The left panel in figure 23 shows the ADC spectrum for a single pixel including the pedestal peak at high ADC values and the signal contributions. The MAPMT gain is then the distance between the single photoelectron and the pedestal peak. The right panel of figure 23 shows the variation in gain g for all 64 channels of the same MAPMT.

The position of the single-photoelectron peak and hence the MAPMT gain varies exponentially with the applied voltage according to

$$g = b + e^{K \cdot U}, \quad (5.2)$$

where U is the applied high voltage and b and K are coefficients determined from the LED data. It was found that the coefficients K are the same for all channels of one MAPMT, whereas the coefficients b reflect the variation in gain shown in the right panel of figure 23. Figure 24 shows the exponential behavior of the measured gain as a function of the applied high voltage together with a fit of the function described in equation 5.2.

Cross-Talk Correction

It is necessary to discriminate cross-talk between neighbouring fibres in the sensitive volume of the SFT and cross-talk on the surface of the MAPMTs. Cross-talk between neighbouring fibres does neither influence the position nor the energy-deposit information provided by the SFT. However, cross-talk on the MAPMT surface leads to wrong hit-position information. In order to disentangle the two sources of cross-talk a sophisticated mapping between the active fibres and the pixels on the

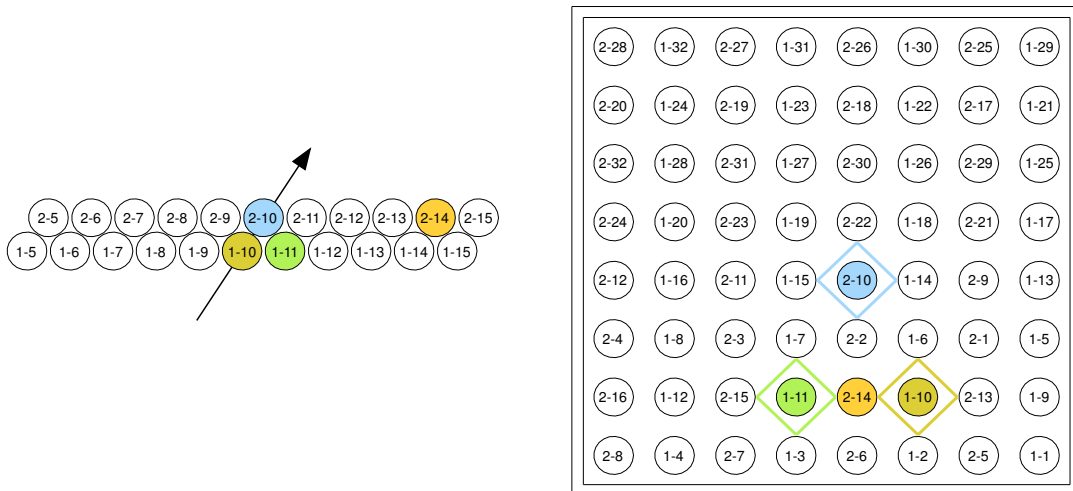


Figure 25. The left panel shows the schematic view of eleven consecutive fibres in a regular and the corresponding shifted layer of a given sub-barrel, indicated by the prefix 1– and 2–, that are connected to the same MAPMT. The mapping on the MAPMT surface is shown in the right panel. A particle traverses fibre 10 in both layers resulting in a direct signal with an additional signal in fibre 1 – 11 due to cross-talk between neighbouring fibres. The signal seen in fibre 2 – 14 originates from cross-talk on the MAPMT surface.

MAPMT surface was developed. In this scheme, neighbouring sensitive fibres are not connected to neighbouring pixels on a MAPMT. The left panel of figure 25 shows eleven consecutive fibres in a regular and the corresponding shifted layer of a given sub-barrel. The mapping of the fibres on the MAPMT surface is shown in the right panel of the figure. The pictures also show the signals originating from an example event, in which a track passes through fibres 1-10 and 2-10, and in the corresponding pixels a signal is observed. In addition, also fibre 1-11 has a signal which is caused by cross-talk between neighbouring sensitive fibres. The signal in fibre 2-14 originates from cross-talk on the PMT surface as can be seen from the right panel of figure 25.

For all pixels with a signal above a threshold of 1.5 photoelectrons, the correction algorithm considers the signals in the direct neighbours as shown in the right panel of figure 25. In the example the signal in pixel 2-14 is below threshold, so only pixels 1-10, 1-11 and 2-10 are corrected for cross-talk. The signal in pixel 2-14 is then split and distributed according to the amplitudes of the signals in pixels 1-10 and 1-11. After the correction pixel 2-14 no longer has a signal, leaving pixel 2-10 with the original signal and pixels 1-10 and 1-11 with an increased signal. For details see reference [33].

Clustering

Similar to the case of SSD, consecutive fibres from a SFT-layer containing signals after the cross-talk correction are combined to clusters. The threshold for combining fibres is imposed by the threshold used in the cross-talk correction algorithm and thus corresponds to 1.5 photoelectrons, as well. In the example, the clustering algorithm produces a cluster containing fibres 1-10 and 1-11 for the lower layer and a cluster with fibre 2-10 for the upper layer. For clusters with more than one fibre, the amplitude-weighted mean fibre number of the cluster is assigned as a virtual fibre number that is later used to determine the precise position of the cluster. For the inner SFT barrel the mean cluster size is 1.2 fibres for all layers, while it is 1.6 fibres for the outer barrel layers.

Energy Calibration

For the purpose of particle identification it is sufficient to extract a relative calibration and equalize the response from all fibres.

The left panel in figure 26 shows the sum of energy deposits in all SFT layers versus the reconstructed momentum, where negative values for the reconstructed momentum correspond to negatively charged particles. The two bands on the positive momentum side originate from positively charged pions and protons and the single band on the negative momentum side corresponds to negatively charged pions. Negatively and positively charged pions with a momentum larger than 0.2 GeV are considered to be minimum-ionizing particles (MIPs) and used in the calibration. Positively charged pions were distinguished from protons by requiring the total energy deposit to lie below the curve shown in the left panel of figure 26.

The right panel in figure 26 displays the energy-deposit distribution after correction for incident angle in units of number of photoelectrons for a single fibre, in the case that in the cluster the fibre was the leading fibre, i.e., the one with the highest signal. A fit of a Landau distribution convoluted with a Gaussian is used to extract the mean energy deposit for MIPs for each fibre. The fit is indicated by the solid line, whereas the mean energy deposit obtained by the fit is shown by

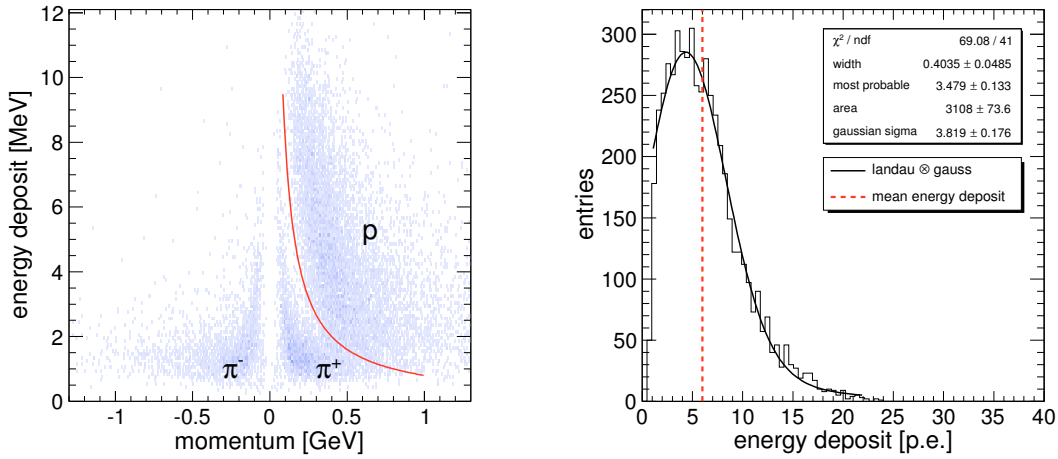


Figure 26. Left: Distribution of the total energy deposit in all SFT layers versus reconstructed momentum. The curve indicates a possible cut to separate protons from positively charged pions. In the calibration pions of both charges were used. Right: Distribution of energy deposits in a single fibre together with a fit of a Landau distribution convoluted with a Gaussian. The fit is used to obtain the numeric mean value of energy deposits for MIPs as indicated by the dashed vertical line.

the vertical dashed line. This mean energy deposit is used for the relative calibration to equalize the response throughout the layers.

Figure 27 shows the mean amplitude of the reconstructed MIPs for all fibres of the inner parallel layer of the inner SFT barrel (left panel) and the parallel layer of the outer barrel (right panel). In the region of fibres 18, 193, 360 and 520 in the inner barrel layer large fluctuations and larger error bars are visible. This is related to the holding structure of the SSD, which limits the acceptance and hence causes a drop in statistics and possibly introduces systematics in the determination of the mean value. For the outer barrel this effect is not as strong, because in the analysis both negatively and positively charged pions are used and the shadowing of the SSD holding structure is less pronounced due to the bending of the particles in the magnetic field. There is also a sub-

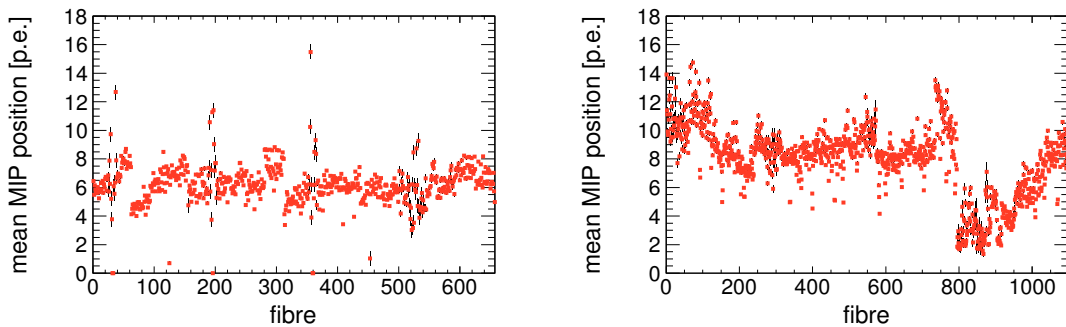


Figure 27. Mean position of the MIP peak for all fibres of the inner parallel layer of the inner barrel (left) and the parallel layer of the outer barrel (right) of the SFT.

structure of 32 consecutive fibres visible in the left panel. Each of these groups corresponds to one bundle of lightguide connections between the active fibres and the MAPMTs. Due to the various bending angles of the lightguides in a bundle, a different amount of light is lost, which results in the observed substructure. In the outer barrel a similar, yet less prominent effect with a substructure of 64 fibres is observed. Most probably the fluctuations are smaller here due to the larger bending radii of the lightguides used for the outer SFT barrel.

In addition, the mean MIP amplitude of the fibres with numbers between 800 and 960 in the outer barrel are smaller compared to the remaining fibres in the layer. With a threshold of 1.5 photoelectrons, this has clearly an influence on the MIP detection efficiency as it will be discussed in section 7.3.

5.3 Photon Detector

By construction, the limited energy-deposition resolution of the PD does not allow the reconstruction of photon energies, due to the given photon-energy sampling fraction between 6% and 10%. However, measured energy deposits are quantities valuable for the selection of photon signals and the identification of charged particles. For signals observed in the PD, the efficiency for photon identification is about 99%, whereas charged-particle identification has an efficiency of around 95% in the case the corresponding track is reconstructed by the SSD and SFT.

Clustering

For the processing of the PD signals, in a first step all strips with an ADC value below threshold (2σ above pedestal) are discarded as well as strips with signals induced by cross-talk in the flat cables. The latter signals are identified as signals with an energy amplitude smaller than half the size of signal amplitudes observed in directly neighbouring flat-cable channels.

In the second step, a MAPMT clustering algorithm is applied that closely follows the one used for the SFT. Initially, the local maxima on the MAPMT are determined. A pair of pixels (associated to the same PD strip) is considered a local maximum, if no higher signal exists in any of its neighbouring pixels, i.e. 8 neighbouring pixel pairs for pixel pairs not located at the edge of the cathode. Then the remaining pixel pairs are examined. Such a pixel pair is considered to be a MAPMT cross-talk hit if its summed energy signal lies below 1.5 MeV and if it corresponds to a PD strip that has no adjacent strip for which a signal is recorded. If any of these two conditions is not satisfied, the pixel pair is promoted to a local maximum. Finally, the energies of the cross-talk hits are added to that of the local maximum. If a cross-talk hit is associated with several local maxima, its energy is shared between them, proportionally to the energy value of each of the associated local maxima. However, since a calibration in terms of photoelectrons was not available for the PD, signal amplitudes in terms of energy units were considered.

In the third step, neighbouring strips in each of the PD layers are combined to clusters. Similar to SSD and SFT, also here the energy contribution from each of the individual strips is appropriately taken into account for the reconstruction of the energy and the energy-weighted position of the clusters. The cluster width amounts in most of the cases to one strip for pions and protons and to one or two strips for photons. From the reconstructed clusters only those with energy values above 1 MeV are stored. The justification for this threshold value lies in the rejection of noise signals,

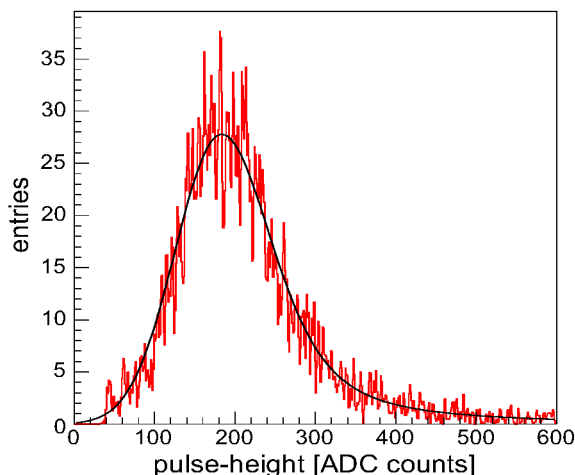


Figure 28. ADC spectrum for energy depositions in the PD by minimum-ionizing particles in units of ADC counts.

which have been shown to be induced by high electron-beam currents and the presence of gas in the target cell.

In the fourth, and last step clusters are associated with tracks reconstructed by the SSD and the SFT, if possible.

Calibration

The calibration of the PD is based on signals from charged pions reconstructed by SSD and SFT with momenta above 0.5 GeV. In this momentum range pions behave as MIPs in the PD. Collisional losses in the scintillating layers result in an energy deposition of 2.1 MeV/cm per active detector layer. The selection of positively charged pions is based on particle-identification information from SSD and SFT.

The calibration follows an iterative procedure: a first calibration is performed on the ADC signals; in a second step, the calibration is based on cross-talk-corrected energy signals.

The signal spectra is fitted with a Landau distribution convoluted with a Gaussian distribution. The numeric mean of this function, determined within certain boundaries, is taken as the calibration point and converted into MeV/cm units based on MC studies. A typical example of such a signal spectrum is shown in figure 28 together with the fit function for signals generated in a PD strip.

The result of the calibration procedure is shown in figure 29 for signals from MIPs. In the figure the mean energy deposition normalized to path length in a cluster of the *A* layer (circle), *B* layer (square), and *C* layer (triangle) is shown as a function of HERMES run number, with the run range corresponding to the entire data collected in the year 2007. As can be seen, the calibrated data show a mean energy-deposition signal of 2.1 MeV/cm, stable over time within the systematic uncertainty of 0.03 MeV/cm.

6. Momentum Reconstruction

The momenta of protons, which can be reconstructed in the RD vary from very low values of about 125 MeV to momenta of up to 1.4 GeV. For protons with momenta above 250 MeV, which reach

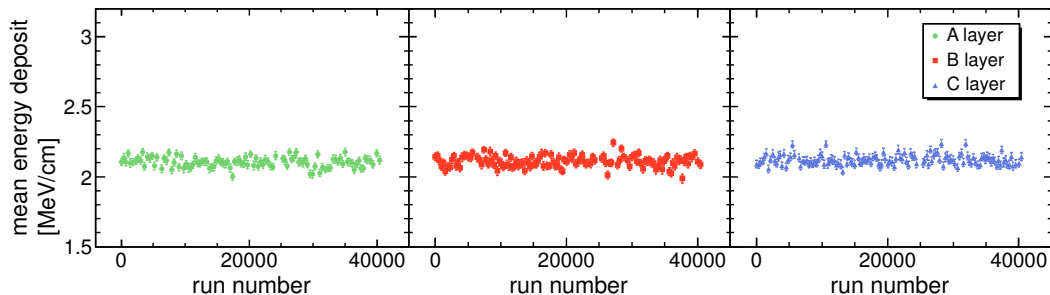


Figure 29. Mean energy deposition of minimum-ionizing particles in a cluster in the *A* layer (circle), *B* layer (square), and *C* layer (triangle) of the PD as a function of run number.

the SFT, momenta can be reconstructed using their deflection in the field of the recoil-detector magnet. Protons with lower momenta are stopped in the outer layer of the SSD. For these protons, the accuracy of the momentum reconstruction using the deflection in the magnetic field is degraded due to the rather small distance of only 1 cm between the two SSD layers. However, the kinetic energy of these protons can be directly reconstructed from the energy deposits in the two SSD layers. The energy deposits can also be employed for protons in the intermediate momentum range, i.e., for protons with high enough momentum to already reach the SFT, in order to improve the momentum resolution.

The track reconstruction algorithm is therefore divided into two stages. In the first stage, a search for tracks with coordinate information in the SSD and SFT layers is performed, and the momentum reconstruction is based solely on the coordinates of the hits. In the second stage, the energy-deposit information is used in addition to the coordinate information assuming that the particle is a proton. Both stages require the coordinate information that is provided by SSD and SFT. This hit-position reconstruction is performed separately prior to the track search.

6.1 Spacepoint Reconstruction

In the following, ‘spacepoint’ refers to a combination of clusters reconstructed in one sub-detector layer, which contains information on the 3D position as well as the energy deposition of the hit.

SSD

With the strips of the p-sides oriented perpendicular to those of the n-sides, the hit position in the sensor plane is obtained directly from the cluster positions given in terms of strip numbers. A constraint on the correlation between measured energy deposits from both sides is applied in order to reduce the number of ghost space points, i.e., the combination of two clusters not belonging to the same track. The energy deposition of a reconstructed spacepoint is calculated as the mean value of the energy deposits given by the two clusters forming the spacepoint. In the case that one sensor side exhibits significantly higher noise, the energy deposit of the formed spacepoint corresponds to the energy deposit of the cluster from the other side.

SFT

In the case of the SFT, the angle between parallel and stereo fibres was 10° . Spacepoints are formed considering geometrically allowed combinations of clusters in the parallel and stereo layers. As the energy deposits from the different layers are only weakly correlated, no hard restrictions can be applied, and unavoidably ghost spacepoints can be created. This has to be taken into account in the subsequent track search. In addition, due to the orientation of the stereo fibres, the resolution in the z -coordinate reconstruction is worse by a factor of $1/\sin(10^\circ) \approx 5.76$ in comparison to the resolution in the xy -plane.

6.2 Track Finding

The track search is performed by combining spacepoints from the SSD and SFT layers. In the first stage of the track search, 4-spacepoint track candidates are considered, i.e., tracks with one spacepoint in each sub-detector layer (inner SSD, outer SSD, inner SFT, and outer SFT). Each track candidate is fitted with a helix hypothesis and accepted if the χ^2 value lies below a certain value. This value is set to 20 according to MC studies, which allows the rejection of most of the ghost tracks with four spacepoints with negligible influence on the efficiency of the track search. From now on, spacepoints belonging to already accepted 4-spacepoint tracks are not considered any longer. During the following stage of the track search, all possible 3-spacepoint combinations are fitted and again tracks with χ^2 below the threshold value are accepted. Finally, all possible 2-spacepoint tracks with hits in the inner and outer SSD layer (including space points belonging to accepted 3-spacepoint tracks) are considered. In the case of 2-spacepoint tracks a χ^2 restriction can not be employed due to the lack of degrees of freedom.

6.3 Momentum Reconstruction by Coordinate Information

The magnetic field of the RD magnet was precisely measured [34] and can be used directly during the momentum reconstruction. The procedure of momentum reconstruction in the magnetic field of the RD is described in the framework of references [35, 36, 37]. MC momentum-resolution studies show that a simple assumption of a homogeneous magnetic field can be used without essential degradation of the accuracy of the momentum reconstruction. Such a simple approach is faster and can be used during track search.

During track fitting, the following function is minimized in the case of independent measurement errors and neglecting multiple scattering:

$$\chi^2 = \sum_{i=1}^N \frac{(S_i^{\text{fit}}(P) - S_i^{\text{meas}})^2}{(\sigma_i^{\text{meas}})^2}, \quad (6.1)$$

where N is the number of measurements, S_i^{meas} and σ_i^{meas} are the measured coordinates and their uncertainties, respectively, and $S_i^{\text{fit}}(P)$ are coordinates as functions of the kinematic parameters P to be fitted to the measured ones. In the momentum reconstruction, the vertex position in the xy -plane is assumed to be the beam position. The beam position is determined by a separate beam-finder computer program for each individual run using 4-spacepoint tracks reconstructed in the recoil detector. The kinematic parameters are chosen to be convenient for a solenoidal magnetic field geometry: $\lambda = 1/p_t = 1/(p \cdot \sin(\theta_v))$, ϕ_v , $\cot(\theta_v)$, and z_v , where p_t is the transverse momentum,

and θ_v , ϕ_v and z_v are respectively the polar angle, azimuthal angle and z coordinate at the vertex position of the track. During minimisation of equation 6.1, the coordinates are expressed as functions of the kinematic parameters in the following way:

$$\phi_{det} = \phi_v - C \cdot R \cdot B \cdot \lambda \cdot \frac{0.3 \text{ GeV}}{200 \text{ T cm}}, \quad (6.2)$$

$$z_{det} = z_v + R \cot(\theta_v), \quad (6.3)$$

where C is the particle charge, B is the magnetic field and R is the distance from a detection layer to the vertex. In order to take multiple scattering into account, equation 6.1 is modified by inclusion of correlation coefficients in the error covariance matrix:

$$\chi^2 = \sum_{i,j=1}^N (S_i^{\text{fit}}(P) - S_i^{\text{meas}}) V_{i,j} (S_j^{\text{fit}}(P) - S_j^{\text{meas}}), \quad (6.4)$$

where $V_{i,j}$ are elements of the covariance matrix V . The covariance matrix is determined from a MC simulation for protons. For pions, the effect of multiple scattering is found to be negligible.

6.4 Momentum Reconstruction Using Energy Deposits in the SSD

For tracks containing hits in the SSD layers, the measured energy deposit in the sensors can be used to improve the momentum reconstruction based on the hit coordinates only. This is achieved by adding an additional term to equation 6.4:

$$\chi^2 = \sum_{i,j=1}^N (S_i^{\text{fit}}(P) - S_i^{\text{meas}}) V_{i,j} (S_j^{\text{fit}}(P) - S_j^{\text{meas}}) + \sum_{i=1}^M \frac{(E_i^{\text{fit}}(P) - E_i^{\text{meas}})^2}{(\sigma_i^{\text{meas}})^2}. \quad (6.5)$$

Here M is the number of energy deposit measurements, E_i^{meas} is the measured energy deposit in a silicon sensor and $E_i^{\text{fit}}(P)$ is the fit value of the energy deposit. The latter is a function (lookup table) of kinematic parameters and is determined from detailed MC studies taking also into account the passive materials [38].

6.5 Alignment

Alignment of SSD and SFT

Knowledge of the detector alignment usually includes internal alignment of individual sub-detectors and relative alignment of sub-detectors. For the alignment procedure several assumptions are made:

- The positions and spacing of strips in each SSD sensor are assumed to be known precisely, as the accuracy of these parameters provided by the manufacturer is much better than required by track reconstruction.
- The intrinsic bending of the SSD sensors is assumed to be negligible.
- The radius of the SFT is assumed to be independent of ϕ angle and z coordinate.

The first step in the alignment procedure is to determine the SFT fibre positions based on data obtained at the DESY22 test beam exploiting 5 GeV electrons. The measurement procedure is described in reference [39]. Straight-track data was used to extract the fibre position along the detector and a lookup table consisting of the ϕ angle and z position of all possible intersections of parallel and stereo fibres was produced.

As a next step, the SSD sensors are positioned relative to each other. Shifts and rotations with respect to the nominal values of each sensor were fitted using an event sample with selected tracks from a cosmic-ray data set collected without magnetic field and reconstructed with a straight-line assumption. The minimization of alignment parameters is performed iteratively by refitting all tracks during each iteration.

With knowledge of the internal alignment of SSD and SFT, both detector components are aligned relative to each other in a final step, using a cosmic-ray event sample with straight tracks. In parallel also small correction of the SFT fibre positions in comparison to the positions obtained from the DESY22 test-beam data are extracted.

The quality of the alignment can be tested using 'residuals' defined as the differences between the hit position in a detection layer calculated from the track parameters and the measured position. As an example, the residuals obtained from a cosmic ray data sample before - using the nominal fibre positions - and after alignment are shown for the outer SFT layer in figure 30. In figures 31

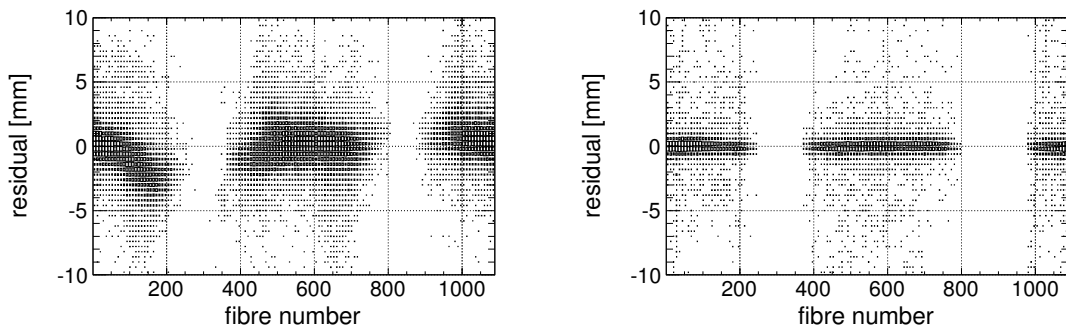


Figure 30. Differences between the hit position in the outer SFT layer calculated from the track parameters and the measured position before (left) and after (right) alignment obtained from a cosmic ray data sample.

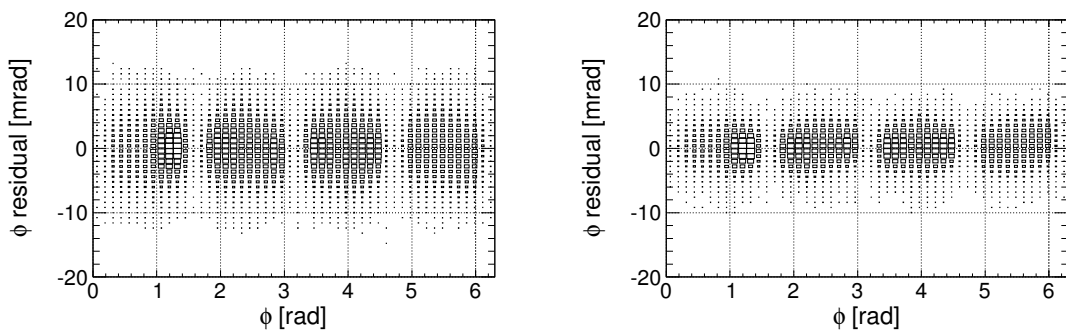


Figure 31. Differences between the ϕ angle of the hit in the inner (left) and outer (right) SSD layers calculated from the track parameters and the measured ϕ angle.

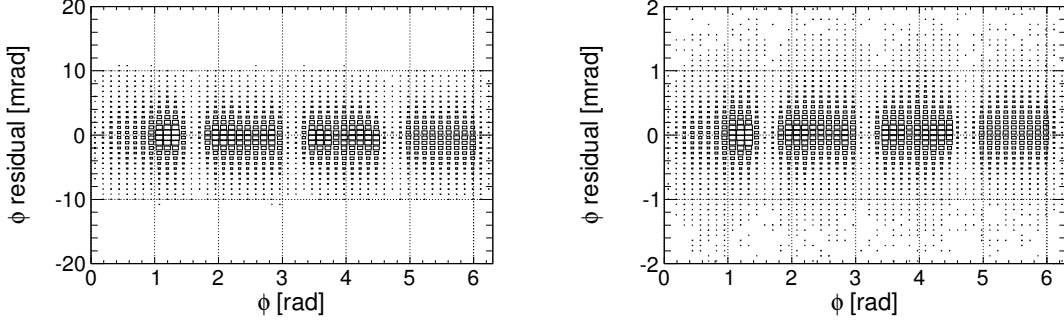


Figure 32. Differences between the ϕ angle of the hit in the inner (left) and outer (right) SFT layers calculated from the track parameters and the measured ϕ angle.

and 32, the azimuthal residuals obtained from experimental data after the alignment are shown for the SSD and SFT layers. In all cases, all four detection layers were included in the track fit. The outer layer of the SFT mainly defines the curvature in the magnetic field and as expected the observed residual is much smaller than for the other layers. A small residual miss-alignment is observed at $\phi \approx 6$ rad even after the iterative alignment procedure that can not be explained and further improved.

Alignment of the PD

The PD is aligned with respect to the SSD and SFT using reconstructed tracks from pions originating from the interaction of the positron beam with the hydrogen target. First, the orientation of each strip of the B and C layers was measured with respect to the beam line and averaged over all strips from the same layer. Secondly, the position along the x and y axis and the rotation in azimuthal angle ϕ of each of the layers was determined, and finally, the measurement of the strip orientation was repeated to check for a possible correlation between the two distinct alignment procedures. Within the uncertainty, no correlation between both procedures was found.

The design value of the radius of each of the PD layers was assumed to be sufficiently accurate by construction. The PD was also assumed not to be inclined with respect to the beam axis, which is a reasonable assumption considering the low θ resolution of the photon detector and results from survey measurements. Finally, the magnetic field was assumed to be homogeneous.

The effect of the PD alignment procedure is shown in figure 33 by means of the $\Delta\phi$ distribution, which represents the difference between the azimuthal angle of the strip center and the azimuthal angle of the track intercept translated along the strip orientation to the upstream end of the detector layer. The vertical dashed lines in the figure delimit one strip pitch. Before the alignment, the mean of the $\Delta\phi$ distribution for π^- amounts to -30 mrad, -35 mrad, and 20 mrad for the A , B , and C layer respectively. After the alignment, the mean of the distribution for π^- (π^+) amounts to 4.2 mrad (-2.8 mrad), 9.6 mrad (-8.7 mrad), and 8.7 mrad (9.8 mrad) for the A , B , and C layer. The deviation from 0 rad is largest for the two outer layers. As the additional knowledge of the z -coordinate of the track intercept with the layer is needed for the B and C layer, and the track's polar angle and z -vertex position are known with less precision than the track's azimuthal angle, an additional bias can be introduced for the two outer layers. Moreover, Monte-Carlo studies

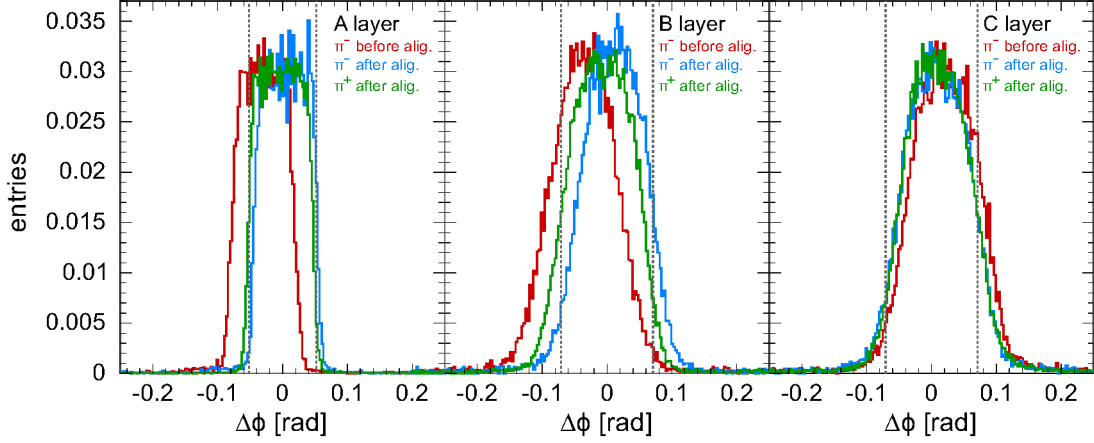


Figure 33. Distributions in $\Delta\phi$ before and after the alignment for the A layer (left), B layer (center), and C layer (right) of the photon detector.

show that the strip orientation can not be determined better than 3.5 mrad/7.0 mrad for a perfectly aligned *B/C* layer, while the layer alignment is limited to 2.8 mrad in ϕ and 0.03 cm in x and y for a precisely known strip orientation. A combination of these various factors can explain the magnitude of the observed shift for each of the three detector layers. This has to be supplemented with a small misalignment in θ of the detector with respect to the beam line of 4.608 ± 0.017 mrad, a value far below the θ -resolution of the photon detector, and with the non-homogeneity of the magnetic field, which is not taken into account. Although the above given arguments can explain the magnitude of the shift, they can not explain the difference in shift of the $\Delta\phi$ distribution between negatively and positively charged pions for the A and B layer. It can be understood, however, if the radii of both layers are underestimated. The construction precision of the photon detector is not better than 0.5 mm for the radius of each layer. The underestimation of the radii of course also contributes to the magnitude of the shift. The inclusion of the layers' radii as free parameters in the layer-alignment procedure can reduce this shift. However, as the magnitude of the shift in either direction does not exceed the shift observed in the C layer, it was decided not to elaborate on this. Further details on the PD alignment procedure can be found in reference [40].

7. Detector Performance

7.1 Momentum Reconstruction

Momentum-resolution studies were performed based on Monte Carlo data samples containing protons and pions. In figures 34 and 35, the accuracy of the momentum and angular reconstruction is presented for protons. Figure 34 shows the momentum reconstruction accuracy using coordinate information only, in comparison with the accuracy of the momentum reconstruction taking into account additionally energy deposits in the SSD. Figure 35 shows azimuthal (left) and polar (right) angle resolutions as calculated using both energy deposits and coordinates. For protons, the angular resolutions deteriorate for momenta below 0.5 GeV because of multiple scattering. For pions,

the momentum resolution is about 12% and the azimuthal (polar) angle resolution is about 4 mrad (10 mrad), with no pronounced dependence on momentum.

7.2 Particle Identification

For each reconstructed track, the energy deposited along the particle's passage through the active detector components can be used to determine the particle type. In the case of tracks that incorporate coordinate information from the four detection layers, a total of six independent energy-deposition measurements are available, coming from the inner and outer SSD layers, and the parallel and stereo layers of the inner and outer SFT barrel. As the protons and pions constitute the predominant statistics, only the separation of these two particle types is considered. Due to the absence of anti-protons, negatively charged tracks are always assumed to be negatively charged pions.

For each energy-deposition measurement and hence each detection layer l , a particle-identification probability PID_l depending on the energy deposition dE and the reconstructed momentum p is calculated according to

$$PID_l(dE; p) = \log_{10} \frac{P_l(dE; \beta\gamma = \frac{p}{m_p})}{P_l(dE; \beta\gamma = \frac{p}{m_\pi})}. \quad (7.1)$$

Here, P_l are the so-called parent distributions, which are energy-deposition distributions normalized to unity, and which depend on the momentum and the particle type. The particle-type dependence in the distributions is eliminated by using a $\beta\gamma = \frac{p}{m_{p/\pi}}$ binning for the energy depositions, namely $\log_{10} \frac{p}{m_{p/\pi}}$.

The combined particle-identification probability is the sum of the probabilities from the individual layers. A cut on the total probability is used to discriminate between charged pions and protons. The actual value of the cut depends on the specific application, i.e., the desired discrimination efficiency and contamination of the other particle type. The particle-identification efficiencies are covered in a subsequent paragraph.

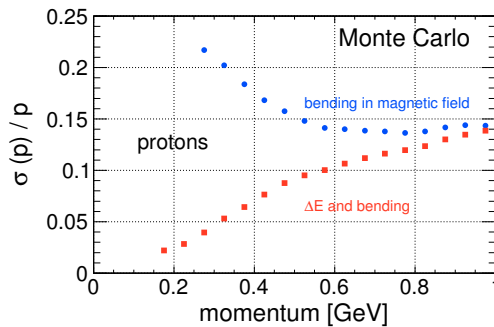


Figure 34. Fractional momentum resolution versus momentum for proton reconstruction by coordinates only (circles) and by energy deposition in the SSD (squares).

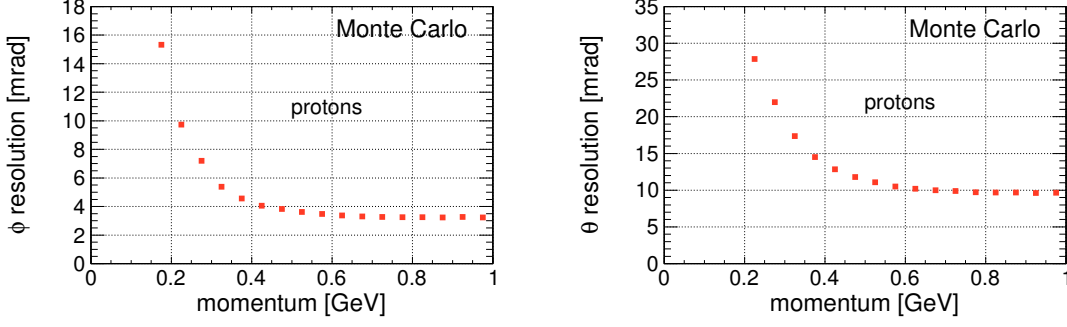


Figure 35. Azimuthal (left) and polar (right) angle resolution versus momentum for protons.

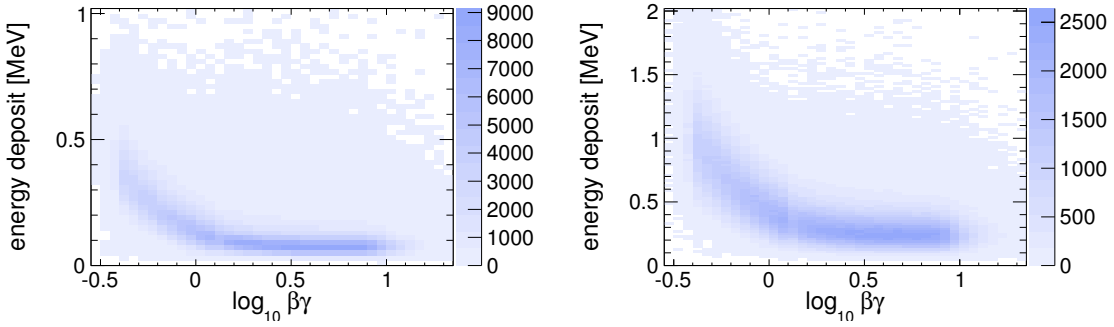


Figure 36. Energy deposit in the inner SSD layer (left) and the inner SFT layer (right) versus $\log_{10}(\beta\gamma)$ for the clean proton and charged pion track sample.

Extraction of Parent Distributions

The quality of the parent distributions P_l is crucial to the performance of the particle identification. In order to avoid effects originating from any remaining miscalibration of the sub-detectors, the distributions were extracted from experimental data instead of Monte Carlo data. This procedure requires clean proton and pion track samples. Events have been chosen with only a single reconstructed track consisting of hits in all four tracking layers. Restrictive cuts on the energy deposit in the other five layers are applied in order to eliminate remaining background when extracting the energy-deposit distributions for a certain detection layer. The energy-deposit distributions versus $\log_{10}(\beta\gamma)$ for both the inner SSD and inner SFT layers are shown in figure 36. Protons with momenta below 1 GeV populate the region $\log_{10}(\beta\gamma) \leq 0.1$, whereas protons with larger momenta and pions with momenta above 0.2 GeV populate the region with $\log_{10}(\beta\gamma)$ larger than 0.1.

For each $\log_{10}(\beta\gamma)$ bin a Landau distribution convoluted with a Gaussian is fit to the energy deposit distribution. The obtained fit parameters are then parameterised as functions of $\log_{10}(\beta\gamma)$. The final parent distributions P_l are obtained from the Landau-Gauss parameterisations. This method ensures also reasonable parent distributions in the transition region at $\log_{10}(\beta\gamma) \approx 0.1$ where a lack of statistics is observed.

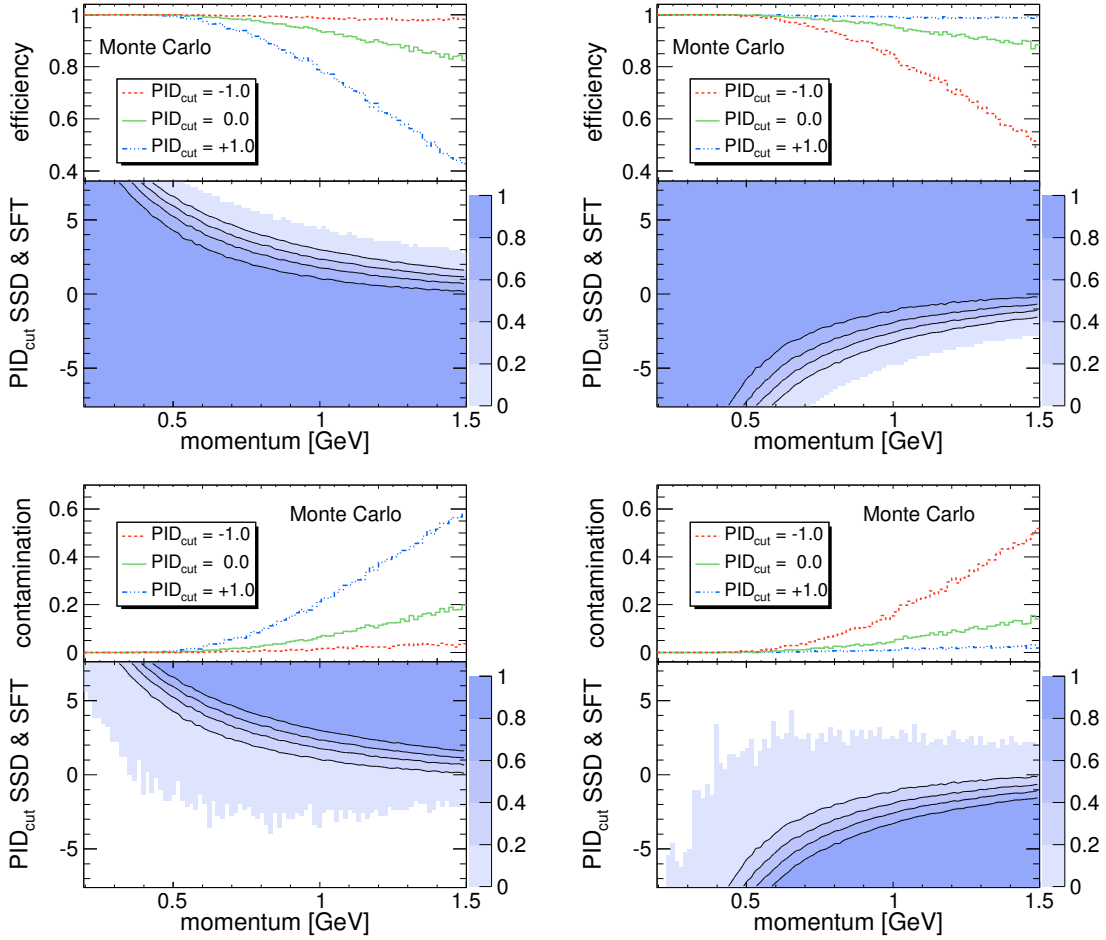


Figure 37. Top-left: Efficiency of the proton identification for tracks consisting of at least three spacepoints. The bottom sub-panel shows the efficiency as a function of particle momentum (x-axis) and a selection cut (PID_{cut}) applied to the combined PID value (y-axis), i.e. the sum of the PID values from the individual detection layers. The top sub-panel depicts the efficiency for three different values of the selection cut above which a particle is deemed to be a proton. Top-right: Efficiency of the pion identification. Here, particles are deemed to be a pion if the combined PID is below the PID_{cut} value. Bottom row: Contamination of a selected particle sample with protons (left) and pions (right) as a function of momentum and combined PID value. The upper sub-panels show the contamination for three different PID_{cut} values.

Particle Identification Efficiency and Contamination

For each reconstructed track, with either three or four spacepoints, the combined particle-identification probability can be calculated from the energy deposits in the layers, the reconstructed momentum and the parent distributions. The combined PID value is used to select protons (charged pions) by requiring the value to be above (below) a certain threshold PID_{cut} . Depending on the actual value of PID_{cut} , selected particle samples contain a certain contamination by the other particle type. In addition, the efficiency of the selection strongly depends on the threshold. Therefore the threshold used to select certain particle types has to be tuned to the specific requirements. In

order to obtain values for the efficiency and contamination levels as a function of the value of PID_{cut} , extensive Monte Carlo studies were performed. The top row of panels in figure 37 shows the efficiency of the proton (left) and pion (right) identification as a function of the reconstructed particle momentum and PID_{cut} value applied to the combined PID (bottom sub-panel) or versus momentum for three different PID_{cut} values (top sub-panel). The bottom row of panels in the figure shows the contamination of a selected track sample with protons (left) and pions (right) as a function of momentum and PID_{cut} value applied to the combined PID (bottom sub-panel) or versus momentum for three different PID_{cut} values (top sub-panel).

For the standard PID_{cut} value of zero, the selection efficiency for protons (top-left panel in figure 37) is close to 1.0 up to a momentum of 0.7 GeV and then it drops to 0.85 at $p \approx 1.5$ GeV. The corresponding contamination with pions can be extracted from the bottom-right panel in the figure. Up to 0.7 GeV the contamination is very low and increases to a value of 0.14 for higher momenta. For pions the situation is very similar. The efficiency is close to 1.0 up to a momentum of 0.6 GeV and drops with increasing momentum to about 0.9 at $p \approx 1.5$ GeV. The respective contamination by protons (bottom-left panel) reaches a value of 0.2 at a momentum of $p \approx 1.5$ GeV. Further details can be found in reference [41].

7.3 Detector Efficiencies

The detection efficiencies of the individual layers are extracted by excluding the layer under study from the track search and reconstruction, and by comparing the number of expected hits with the number of detected hits in a narrow special window in that layer. As the SSD was not designed for high efficiency for MIPs but rather for low energy recoiling protons, the efficiency shows a strong dependence on the particle momentum and type. In order to eliminate the particle-type dependence, a binning of the extracted efficiency values in $\log_{10}(\beta\gamma)$ instead of momentum and particle type is used for SSD and SFT.

Efficiency of the SSD

The efficiency of the SSD is extracted for hits, clusters and spacepoints. In the case of the inner (outer) sensors the hit predictions are obtained from an interpolation of the tracks reconstructed from the hits in the outer (inner) SSD and inner SFT, and the beam constraint to the layer under study. Figure 38 shows the cluster efficiency for both p- and n-sides of one inner and one outer sensor for two $\log_{10}(\beta\gamma)$ ranges. The solid markers for which $\log_{10}(\beta\gamma) < -0.1$ constitute the bulk of the proton statistics. In this region the cluster efficiency for all sensors is above 99%. The panel for the inner p-side efficiency misses data points for low and high strip numbers. The reason for this is the smaller ϕ acceptance of the corresponding outer sensor and therefore absence of statistics in these strip regions in the inner sensors. For $\log_{10}(\beta\gamma) > -0.1$, which corresponds to protons with momenta above 800 MeV and most of the pion statistics, the cluster efficiency is lower. The results shown in figure 38 represent sensors with rather high cluster efficiencies for pions. Due to the fact that the hardware threshold was set to 50% of the most probable energy deposit of a MIP, the cluster efficiency is strongly affected by small variations in the gain and linearities of the high-gain readout channel. For some sensors the MIP efficiency was as low as 30%. The lower left panel of figure 38 also shows a drop in efficiency for both $\log_{10}(\beta\gamma)$ ranges at around strip 80. This is

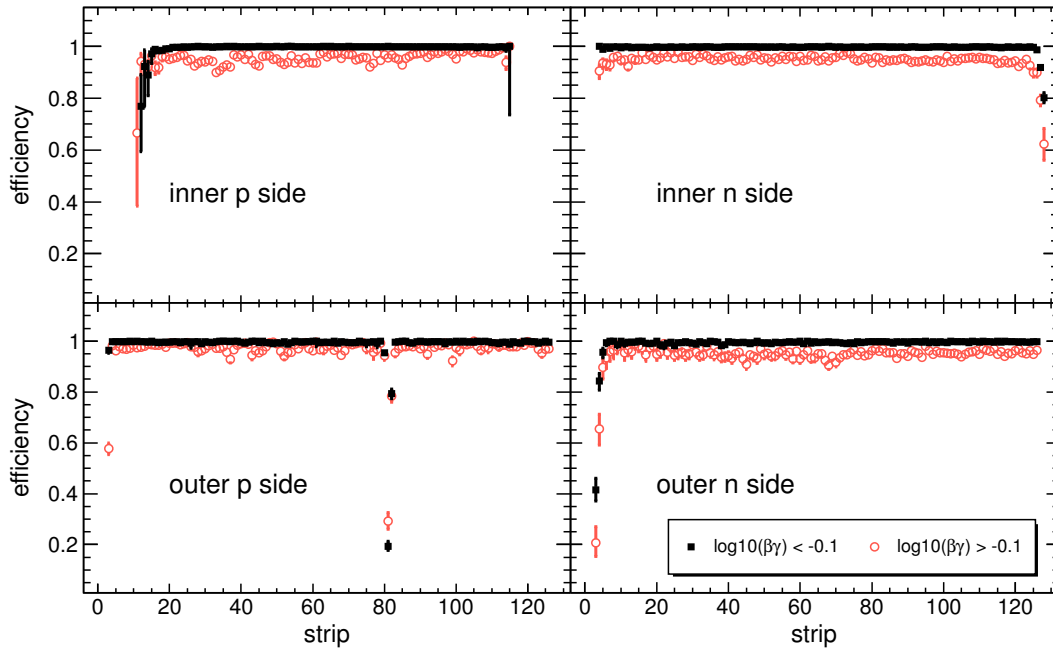


Figure 38. Cluster efficiency for the p- and n-sides of one of the inner SSD sensors (top) and one of the outer sensors (bottom) for two ranges in $\log_{10}(\beta\gamma)$. The range $\log_{10}(\beta\gamma) < -0.1$ constitutes the bulk of the proton statistics.

caused by a dead strip with zero efficiency which is smeared over a few strips due to the limited position resolution.

Efficiency of the SFT

Very similar to the case of the SSD, the efficiency of the SFT is determined for individual fibres. The cluster efficiencies as a function of fibre number are shown in figure 39 for two different $\log_{10}(\beta\gamma)$ regions and the four layers of the SFT: inner parallel, inner stereo, outer parallel and outer stereo. The gaps with undefined efficiency are caused by lack of statistics due to shadowing by the SSD holding structure. The inner SFT layers have an efficiency of above 95% in the region $\log_{10}(\beta\gamma) < 0.1$ and above 90% for the high- $\log_{10}(\beta\gamma)$ region. In general, the outer layers show a very similar behavior. However, the outer parallel layers have a very low efficiency in the region between fibres 850 and 950 due to two not properly functioning MAPMTs. As a consequence, also the determination of the efficiency of the other layers suffers from this effect by lack of statistics and lower quality tracks. Moreover, the coverage in the angle ϕ of the fibres connected to the non working MAPMTs has an overlap with the ϕ acceptance of the non-fully functioning outer SSD module (see section 4.2) which causes an even larger decrease in track quality when neglecting the layer under study during track search and fit. The combined effect on the efficiencies can be seen for the parallel layer of the outer SFT at fibres 800 and 900, as well as in the inner layers in the region of fibres 550 through 600. Details on the efficiency of the SFT can be found in references [39] and [41].

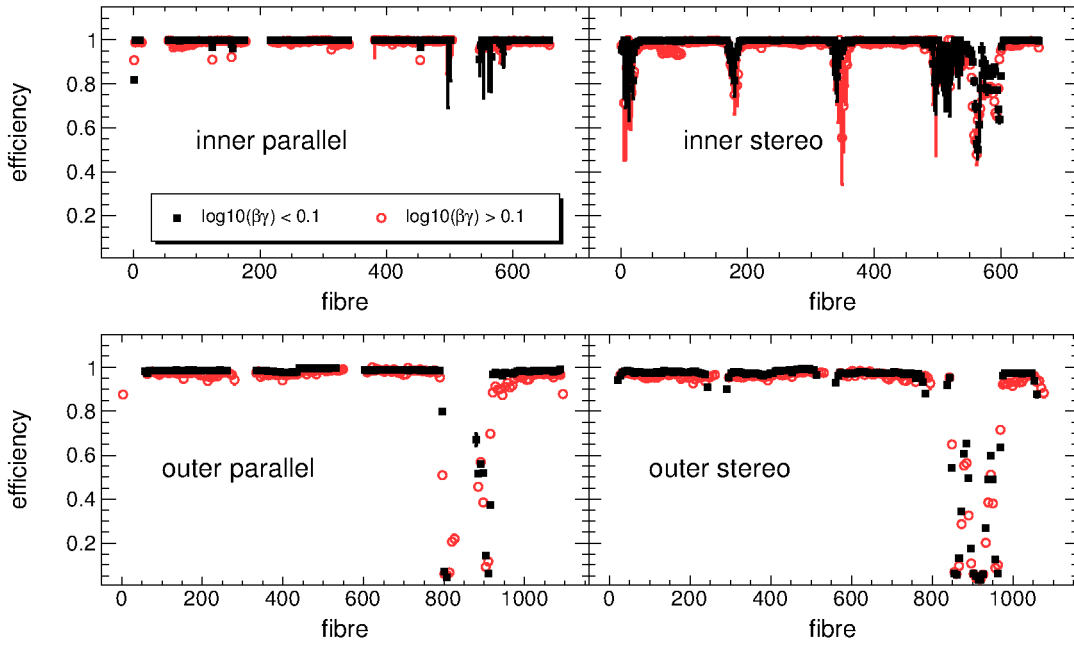


Figure 39. Efficiency of the SFT layers for two regions of $\log_{10}(\beta\gamma)$. The different panels show the individual layers of the SFT.

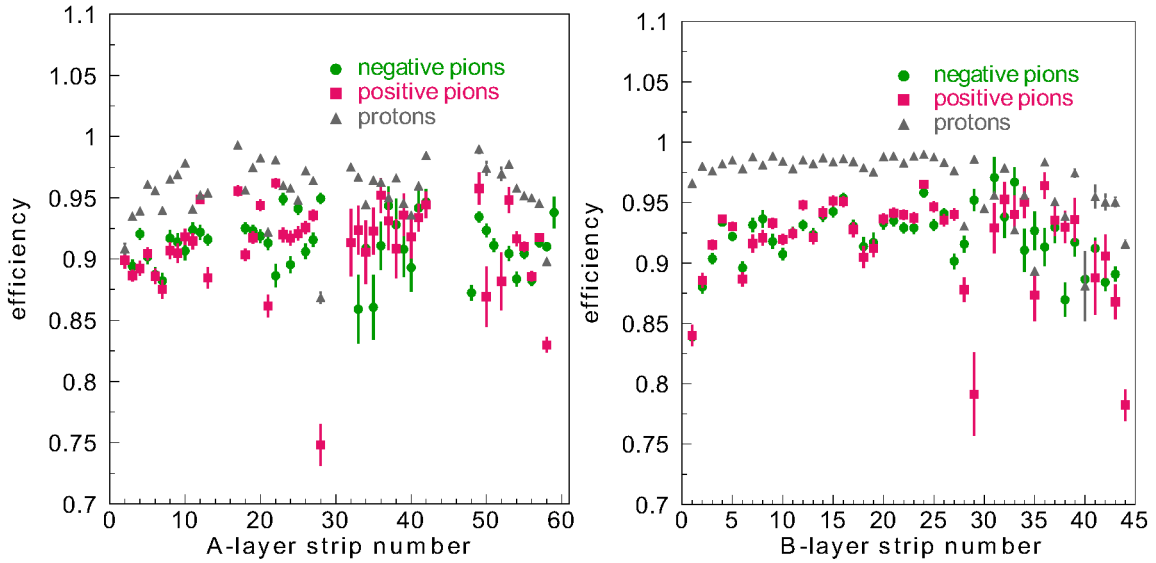


Figure 40. Efficiency of the A layer (left) and B layer (right) of the PD for charged pions and protons with momenta between 0.6 GeV and 0.7 GeV.

Efficiency of the PD

The detection efficiencies of the individual PD layers are studied using tracks reconstructed by both the SSD and SFT, and by requiring a signal in the PD layers not under investigation. The

efficiencies are presented in figure 40 for signals from positively and negatively charged pions and from protons in the *A* layer and *B* layer. Since the *C* layer is the outermost active detector component, it is not possible to distinguish between particles that passed through the *C* layer and those that stopped before the *C* layer. Therefore, the efficiency for the *C* layer is not determined to the same extent. In addition, the track selection limits the acceptance for the extraction of the PD efficiency.

As can be seen in figure 40, on average no difference in detection efficiency for positively and negatively charged pions is observed. For strips located around the gap in between two silicon strip modules, the bending in opposite direction of the positively and negatively charged particles in the magnetic field together with the track selection leads to small differences. Apart from these edge effects and not considering the problematic region with the not fully functioning SSD module (see section 4.2) and the non-working SFT MAPMTs (see section 7.3), which affects strips 46–50 of the *A*-layer and strips 1–3 and 38–44 of the *B*-layer, the detection efficiency shows no dependence on either the momentum or the charge of the pions. It is about 92% for both layers.

As expected, the detection efficiency for protons lies well above the detection efficiency for pions. A higher proton-detection efficiency in the *B* layer than in the *A* layer is observed, because of the requirement of a signal in the *A* and *C* layer or in the *B* and *C* layer, respectively. This requirement, introduced in order to reject noise hits, results in a larger average energy deposition in the *B* layer than in the *A* layer.

8. Event Selection with the Recoil Detector

In the following chapter, details about the selection of DVCS events are presented. In a similar manner, events from other exclusive processes can be selected with the use of RD information.

DVCS event candidates are selected requiring the detection of exactly one scattered electron or positron and exactly one photon measured in the forward spectrometer. In addition, information on all tracks reconstructed in the recoil detector is used in the analysis.

In the left panel of figure 41, the difference between the proton transverse momentum reconstructed with the RD and the missing transverse momentum calculated using information from only the forward spectrometer is presented versus the difference between reconstructed and calculated azimuthal angles. The right panel of figure 41 shows the distribution of the squared missing mass

$$M_X^2 = (k + p - k' - q')^2, \quad (8.1)$$

calculated using the 3-momenta of the scattered lepton and the real photon (q'). By applying a cut on these distributions one can select DVCS events and suppress background events. However, for the selection of "pure" DVCS events, i.e., DVCS events where the proton stays in its ground state, this simple approach is not optimal and an alternative approach, kinematic event fitting, is used instead.

In the kinematic event fitting approach, all available information from the detected particles is combined under a certain hypothesis on the event kinematics. In the case of DVCS, four kinematic constraints can be constructed from the energy-momentum conservation assuming electron, photon and proton as particle types and absence of other particles in the final state. Technically (and in

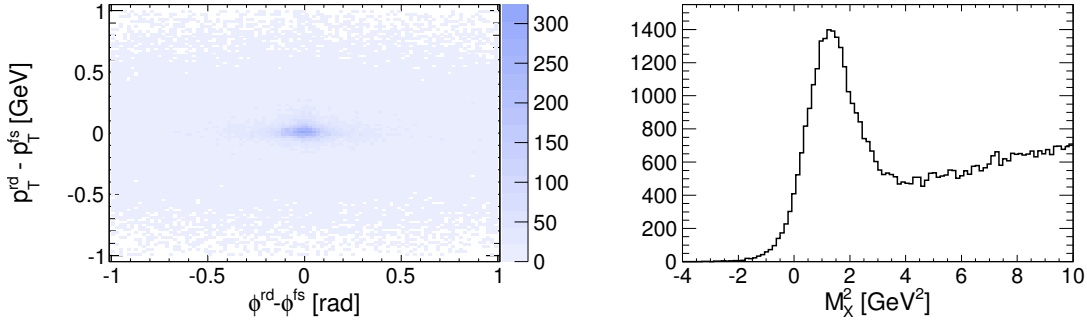


Figure 41. Left panel: The difference between the transverse momentum of the proton reconstructed in the RD and the transverse momentum calculated from the measured 3-momenta of the scattered lepton and real photon versus the difference between the reconstructed and calculated azimuthal angles. Right panel: Squared missing mass calculated from the measured 3-momenta of the scattered lepton and real photon.

the case that the measured kinematic parameters are not correlated) a χ_{kin}^2 probability distribution function

$$\chi_{\text{kin}}^2 = \sum_{i=1}^n (r_i^{\text{fit}} - r_i^{\text{meas}})^2 / \sigma_i^2 \quad (8.2)$$

is constructed under the conditions that

$$f_j = f_j(r_1^{\text{fit}}, r_2^{\text{fit}}, \dots, r_n^{\text{fit}}) = 0, \quad j = 1, \dots, m. \quad (8.3)$$

Here f_j are (usually nonlinear) functions of kinematic parameters, r_i^{meas} and r_i^{fit} are the measured and fit kinematic parameters, respectively, σ_i are measurement uncertainties, n is the number of kinematic parameters and m is the number of kinematic constraints.

In the case of DVCS, the following nine kinematic parameters are chosen:

$$r = \left\{ \frac{p_x^e}{p_z^e}, \frac{p_y^e}{p_z^e}, \frac{1}{p^e}, \frac{p_x^\gamma}{p_z^\gamma}, \frac{p_y^\gamma}{p_z^\gamma}, \frac{1}{p^\gamma}, \phi^p, \theta^p, \frac{1}{p^p \cdot \sin(\theta^p)} \right\}.$$

Here p_x^e, p_y^e, p_z^e, p^e are the x, y, z components and absolute value of the momentum of the scattered positron, $p_x^\gamma, p_y^\gamma, p_z^\gamma, p^\gamma$ the x, y, z components and absolute value of the momentum of the real photon and ϕ^p, θ^p and p^p the azimuthal and polar angles and the absolute value of the momentum of the recoiling proton.

The minimisation of the χ_{kin}^2 function with constraints can be achieved by the method of penalty functions (see, e.g. reference [42] for details). In this method, penalty terms are added to the chi-square function

$$\chi_{\text{pen}}^2 = \chi_{\text{kin}}^2 + T \cdot \sum_{j=1}^m f_j^2 / (\sigma_j^f)^2, \quad (8.4)$$

where σ_j^f is the error of the j -th constraint and T is a constant penalty number. For sufficiently large T , the constraints are automatically satisfied after convergence of the minimization procedure.

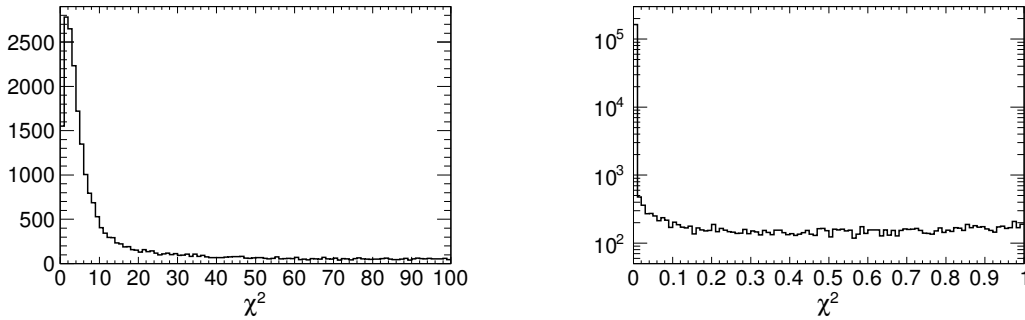


Figure 42. Left panel: Distribution of χ^2_{kin} from kinematic event fitting for DVCS event candidates. Right panel: Probability distribution corresponding to the χ^2 distribution.

The measurement uncertainties are extracted from data sets generated by Monte Carlo. The momentum dependence of the measurement errors is parametrized for electrons and photons measured in the forward spectrometer and protons registered in the RD. Small corrections of the measurement uncertainties are applied for experimental data based on the observed difference between data and Monte Carlo.

The resulting χ^2_{kin} -distribution from kinematic event fitting is displayed in the left panel of figure 42 for DVCS event candidates with one lepton and one photon measured in the forward spectrometer and a proton candidate registered in the RD. In the right panel the fit probability distribution is presented, which corresponds to the χ^2 -distribution for four degrees of freedom. In the ideal case of Gaussian distributions of the measurement uncertainties σ_i and absence of background, this probability is expected to be uniformly distributed between zero and unity.

In the case that there are multiple proton track candidates reconstructed in combination with the scattered electron and the real photon, the proton candidate that resulted in the smallest χ^2_{kin} -value is selected. The probability calculated from χ^2_{kin} that a particular event satisfied the DVCS hypothesis is required to be larger than 0.01, a value that is adequate to ensure negligible background contamination. The performance of this event selection is studied using an appropriate mixture of simulated signal and background events [43, 44]. Events satisfying all other previously mentioned constraints are found to be selected with high efficiency (83%) and background contamination less than 0.2%.

In figures 43 and 44, results of the event selection using kinematic event fitting are presented. A clear peak in the difference between the transverse momentum of the proton reconstructed in the RD and the transverse missing momentum calculated from the measured 3-momenta of the scattered lepton and real photon as well as in the difference between the reconstructed and calculated azimuthal angles is observed (left panel of figure 43 and both panels of figure 44). From the missing-mass distributions shown in the right panel of figure 43, only the one with the fit probability above 0.01 (solid line) shows Gaussian behavior, confirming a clear and background-free selection of the pure DVCS sample. Such a distinction performance is not possible with applying simple constraints on kinematic distributions.

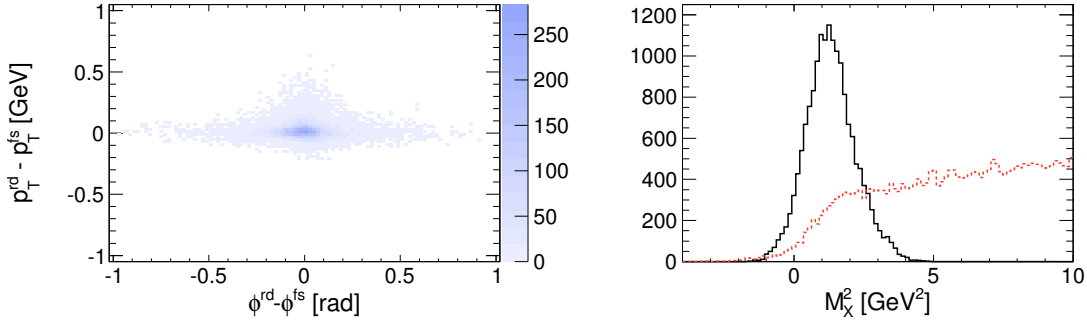


Figure 43. Left panel: The difference between the transverse momentum of the proton reconstructed in the RD and the one calculated using only information from the forward spectrometer versus the difference between reconstructed and calculated azimuthal angles for DVCS events selected using kinematic event fitting with the fit probability above 0.01. Right panel: Squared missing mass calculated from the measured 3-momenta of the scattered lepton and real photon for selected DVCS events with the fit probability above 0.01 (solid line) and rejected events with the fit probability below 0.01 (dashed line).

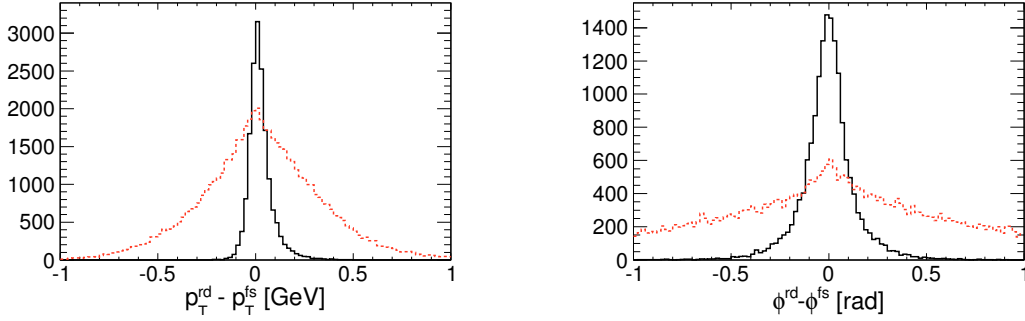


Figure 44. Left panel: The difference between the transverse momentum of the proton reconstructed in the RD and the one calculated using only information from the forward spectrometer for selected DVCS events with the fit probability above 0.01 (solid line) and rejected events with the fit probability below 0.01 (dashed line). Right panel: The difference between reconstructed and calculated azimuthal angles for selected DVCS events with the fit probability above 0.01 (solid line) and rejected events with the fit probability below 0.01 (dashed line).

9. Conclusion

The main purpose of the RD was the registration of protons and charged pions with momenta from 0.125 GeV to 1.4 GeV and large polar angles in order to measure the complete kinematics of hard exclusive processes in electroproduction. For this aim, a set of silicon strip detectors situated inside the HERA beam vacuum, a scintillating-fibre tracker and a photon detector, all surrounded by a superconducting magnet with a field strength of 1 T, were installed in the HERMES target region. Commissioning of the detector started in spring 2006 when part of the detector was already operational and finished in fall 2006 resulting in stable running of the detector until the HERA shutdown in June of 2007. All detector components were calibrated, detector efficiencies were studied and the alignment of all subdetectors was performed based on cosmic ray and experimental

data from normal detector running periods. The tracking and momentum-reconstruction algorithms developed allow for a momentum reconstruction in a wide momentum range. For low-momentum protons, in addition to coordinate information from the SSD and SFT, energy deposits in the SSD are used to improve the momentum reconstruction. The main purpose of the PD was the detection of photons, but it was also capable of detecting high-energetic protons and charged pions. The particle-identification techniques, which use energy deposits in the SSD, SFT and PD, allow for a reliable selection of protons and charged pions with momenta below 0.7 GeV.

First results on single-charge beam-helicity asymmetry in deeply virtual Compton scattering using the RD were recently obtained [45]. As intended, the use of the RD allows a suppression of the background to a negligible level.

Acknowledgments

We gratefully acknowledge the DESY management for its support and the staff at DESY and the collaborating institutions for their significant effort. This work was supported by the Ministry of Economy and the Ministry of Education and Science of Armenia; the FWO-Flanders and IWT, Belgium; the Natural Sciences and Engineering Research Council of Canada; the National Natural Science Foundation of China; the Alexander von Humboldt Stiftung, the German Bundesministerium für Bildung und Forschung (BMBF), and the Deutsche Forschungsgemeinschaft (DFG); the Italian Istituto Nazionale di Fisica Nucleare (INFN); the MEXT, JSPS, and G-COE of Japan; the Dutch Foundation for Fundamenteel Onderzoek der Materie (FOM); the Russian Academy of Science and the Russian Federal Agency for Science and Innovations; the Basque Foundation for Science (IKERBASQUE) and the UPV/EHU under program UFI 11/55; the U.K. Engineering and Physical Sciences Research Council, the Science and Technology Facilities Council, and the Scottish Universities Physics Alliance; the U.S. Department of Energy (DOE) and the National Science Foundation (NSF); as well as the European Community Research Infrastructure Integrating Activity under the FP7 "Study of strongly interacting matter (HadronPhysics2, Grant Agreement number 227431)".

References

- [1] K. Ackerstaff et al., *The HERMES Spectrometer*, *Nucl. Instrum. Meth. A* **417** (1998) 230–265
- [2] D. Müller et al., *Wave Functions, Evolution Equations and Evolution Kernels from Light-Ray Operators of QCD*, *Fortschritte der Physik* **42** (1994) 101–141
- [3] A. V. Radyushkin, *Scaling limit of deeply virtual compton scattering*, *Phys. Lett. B* **380** (1996) 417–425
- [4] X. Ji, *Deeply virtual Compton scattering*, *Phys. Rev. D* **55** (1997) 7114–7125
- [5] X. Ji, *Viewing the Proton through "Color" Filters*, *Phys. Rev. Lett.* **91** (2003) 062001
- [6] A. V. Belitsky, X. Ji, and F. Yuan, *Quark imaging in the proton via quantum phase-space distributions*, *Phys. Rev. D* **69** (2004) 074014
- [7] X. Ji, *Gauge-Invariant Decomposition of Nucleon Spin*, *Phys. Rev. Lett.* **78** (1997) 610–613

- [8] M. Burkardt, *Impact parameter dependent parton distributions and off-forward parton distributions for $\zeta \rightarrow 0$* , *Phys. Rev. D* **62** (2000) 071503, Erratum-ibid. *Phys. Rev. D* **66** (2002) 119903(E)
- [9] A. Airapetian et al., [HERMES Collaboration], *Measurement of azimuthal asymmetries with respect to both beam charge and transverse target polarization in exclusive electroproduction of real photons*, *JHEP* **06** (2008) 066
- [10] A. Airapetian et al. [HERMES Collaboration], *Separation of contributions from deeply virtual Compton scattering and its interference with the Bethe-Heitler process in measurements on a hydrogen target*, *JHEP* **11** (2009) 083
- [11] A. Airapetian et al. [HERMES Collaboration], *Exclusive lepton production of real photons on a longitudinally polarised hydrogen target*, *JHEP* **06** (2010) 019
- [12] A. Airapetian et al. [HERMES Collaboration], *Beam-helicity and beam-charge asymmetries associated with deeply virtual Compton scattering on the unpolarised proton*, *JHEP* **07** (2012) 032
- [13] B. Krauß, *Deeply Virtual Compton Scattering and the HERMES-Recoil Detector*, Friedrich Alexander Universität Erlangen-Nürnberg, Erlangen, Germany, DESY-THESIS-2005-008, 2005
- [14] T. J. O'Neill et al., *Development of the TIGRE Compton Telescope for Intermediate-Energy Gamma-Ray Astronomy*, *IEEE Trans. Nucl. Sci.* **50** (2003) 251–257
- [15] *Machinable Aluminium Nitride Ceramic SHAPALTM-M soft technical data sheet*, Goodfellow Cambridge Limited
- [16] W. Fallow-Burghardt, *A CMOS Mixed-Signal Readout Chip for the Microstrip Detectors of HERA-B*, Ruprecht-Karls-Universität Heidelberg, Heidelberg, Germany, 1998
- [17] M. Reinecke et al., *A Silicon Strip Recoil Detector for Momentum Measurement and Tracking at HERMES*, *IEEE Trans. Nucl. Sci.* **51** (2004) 1111–1116
- [18] A. Vandenbroucke, *Exclusive π^0 Production at HERMES: Detection - Simulation - Analysis*, Ghent University, Ghent, Belgium, DESY-THESIS-2007-003, 2007
- [19] N. C. Pickert, *Commissioning of the Recoil Silicon Detector for the HERMES Experiment*, Friedrich Alexander Universität Erlangen-Nürnberg, Erlangen, Germany, DESY-THESIS-2008-005, 2008
- [20] J. J. M. Steijger, *The lambda wheels, a silicon vertex detector for HERMES*, *Nucl. Instrum. Meth. A* **453** (2000) 98–102
- [21] M. Hoek, *Design and Construction of a Scintillating Fibre Tracker for Measuring Hard Exclusive Reactions at HERMES*, Justus-Liebig Universität Gießen, Gießen, Germany, DESY-THESIS-2006-027, 2006
- [22] M. Hoek et al., *Performance and response of scintillating fiber modules to protons and pions*, *Nucl. Instrum. Meth. A* **572** (2007) 808–816
- [23] *Multi-anode Photomultiplier Tube Assembly H7546 data sheet*, Hamamatsu Photonics Corporation, 2000
- [24] Y. Van Haarlem, *The HERMES Recoil Photon-Detector and Nuclear p_T -Broadening at HERMES*, Ghent University, Ghent, Belgium, DESY-THESIS-2007-033, 2007
- [25] A. Kastenmüller et al., *Fast detector readout for the HADES-RICH*, *Nucl. Instrum. Meth. A* **433** (1999) 438–443
- [26] *BC-400, BC-404, BC-408, BC-412, BC-416 Premium Plastic Scintillators data sheet*, Saint-Gobain Ceramics & Plastics, Inc, 2005–2008

- [27] T. Keri, *Detection of Exclusive Reactions in the Hermes Recoil Fiber Tracker*, Justus-Liebig Universität Gießen, Gießen, Germany, DESY-THESIS-2008-021, 2008
- [28] C. Vogel, *Kalibration von Siliziumdetektoren für den HERMES Rückstoßdetektor*, Friedrich Alexander Universität Erlangen-Nürnberg, Erlangen, Germany, 2008
- [29] I. Vilardi, *Detection of Low Momentum Protons with the New HERMES Recoil Detector*, University of Bari, Bari, Italy, DESY-THESIS-2008-033, 2008
- [30] D. Zeiler, *Deeply Virtual Compton Scattering off an Unpolarized Hydrogen Target at the HERMES Experiment*, Friedrich Alexander Universität Erlangen-Nürnberg, Erlangen, Germany, DESY-THESIS-2009-041, 2009
- [31] S. Agostinelli et al., *GEANT4 - a simulation toolkit*, *Nucl. Instrum. Meth. A* **506** (2003) 250–303
- [32] J. Allison et al., *Geant4 developments and applications*, *IEEE Trans. Nucl. Sci.* **53** (2006) 270–278
- [33] W. Yu, *Beam-Helicity Azimuthal Asymmetry measured with the Recoil Detector in Exclusive Electroproduction of Real Photons at HERMES*, Justus-Liebig Universität Gießen, Gießen, Germany, DESY-THESIS-2009-042, 2009
- [34] M. Statera, *Superconducting Magnetic Systems for High Energy Polarized Physics*, Università delgi Studi di Ferrara, Ferrara, Italy, DESY-THESIS-2006-069, 2006
- [35] A. Osborne, *Exclusive ρ^0 Cross Section Ratios in Deuterium and Hydrogen Targets*, University of Glasgow, Glasgow, United Kingdom, DESY-THESIS-2006-024, 2006
- [36] G. D. Hill, *Deeply Virtual Compton Scattering off Unpolarised Deuterium at HERMES*, University of Glasgow, Glasgow, United Kingdom, DESY-THESIS-2008-035, 2008
- [37] D. F. Mahon, *Deeply Virtual Compton Scattering off Longitudinally Polarised Protons at HERMES*, University of Glasgow, Glasgow, United Kingdom, DESY-THESIS-2010-023, 2010
- [38] J. R. T. Burns, *Deeply Virtual Compton Scattering off an Unpolarised Hydrogen Target at HERMES*, University of Glasgow, Glasgow, United Kingdom, DESY-THESIS-2010-036, 2010
- [39] R. F. Perez-Benito, *Exclusive ρ^0 Production Measured with the HERMES Recoil Detector*, Justus-Liebig Universität Gießen, Gießen, Germany, DESY-THESIS-2010-052, 2010
- [40] C. Van Hulse, *The HERMES recoil photon detector and the study of deeply virtual Compton scattering*, Ghent University, Ghent, Belgium, DESY-THESIS-2011-008, 2011
- [41] X.-G. Lu, *The HERMES Recoil Detector: Particle Identification and Determination of Detector Efficiency of the Scintillating Fiber Tracker*, Universität Hamburg, Hamburg, Germany, DESY-THESIS-2009-043, 2009
- [42] S. N. Dymov, V. S. Kurbatov, I. N. Silin, S. V. Yaschenko, *Constrained minimization in the C++ environment*, *Nucl. Instrum. Meth. A* **440** (2000) 431–437
- [43] G. Ingelman, A. Edin, J. Rathsman, *LEPTO 6.5 - A Monte Carlo Generator for Deep Inelastic Lepton-Nucleon Scattering*, *Comput. Phys. Commun.* **101** (1997) 108
- [44] V. A. Korotkov and W. D. Nowak, *Future Measurements of Deeply Virtual Compton Scattering at HERMES*, *Eur. Phys. J. C* **23** (2002) 455
- [45] A. Airapetian et al. [HERMES Collaboration], *Beam-helicity asymmetry arising from deeply virtual Compton scattering measured with kinematically complete event reconstruction*, *JHEP* **10** (2012) 042